J. Fluid Mech. (2002), *vol.* 462, *pp.* 1–30.
DOI: 10.1017/S0022112002008467 Printed in the United Kingdom

A new Boussinesq method for fully nonlinear waves from shallow to deep water

By P. A. MADSEN[1], H. B. BINGHAM[1] AND HUA LIU[2]

[1]Department of Mechanical Engineering, Technical University of Denmark, DK-2800 Kgs. Lyngby, Denmark

[2]Institute of Water Resources and Environmental Research, Shanghai Jiao Tong University, Shanghai 200030, P. R. China

(Received 10 March 2001 and in revised form 13 December 2001)

A new method valid for highly dispersive and highly nonlinear water waves is presented. It combines a time-stepping of the exact surface boundary conditions with an approximate series expansion solution to the Laplace equation in the interior domain. The starting point is an exact solution to the Laplace equation given in terms of infinite series expansions from an arbitrary z-level. We replace the infinite series operators by finite series (Boussinesq-type) approximations involving up to fifth-derivative operators. The finite series are manipulated to incorporate Padé approximants providing the highest possible accuracy for a given number of terms. As a result, linear and nonlinear wave characteristics become very accurate up to wavenumbers as high as $kh = 40$, while the vertical variation of the velocity field becomes applicable for kh up to 12. These results represent a major improvement over existing Boussinesq-type formulations in the literature. A numerical model is developed in a single horizontal dimension and it is used to study phenomena such as solitary waves and their impact on vertical walls, modulational instability in deep water involving recurrence or frequency downshift, and shoaling of regular waves up to breaking in shallow water.

1. Introduction

The classical Boussinesq equations for water waves (see e.g. Peregrine 1967) incorporate only weak dispersion and weak nonlinearity and in practice their range of applicability is limited to $kh < 0.75$ (where k is wavenumber and h water depth). Generally, the weak dispersion is the most critical limitation as it directly affects the accuracy of the wave celerity, which is crucial for most wave dynamics. This shortcoming has attracted considerable attention in the last 10–15 years, and a number of enhanced and higher-order Boussinesq equations have been formulated to improve both linear and nonlinear properties. As a result the best forms have extended the linear range of applicability up to $kh \approx 6$ (see e.g. Madsen & Schäffer 1998; Gobbi, Kirby & Wei 2000). Weak nonlinearity is also a shortcoming, and although several recent papers have claimed to present so-called fully nonlinear Boussinesq formulations, most of them have incorporated linear far better than nonlinear characteristics (see e.g. Wei *et al.* 1995; Madsen & Schäffer 1998, 1999; and Gobbi *et al.* 2000).

A breakthrough, treating nonlinearity, was made by Agnon, Madsen & Schäffer (1999, referred to as AMS99 in the following). They presented a new procedure by which it is possible to achieve the same accuracy in nonlinear properties as in

linear properties. Their procedure is based on an exact formulation of the boundary conditions at the free surface and at the sea bottom combined with an approximate solution to the Laplace equation given in terms of truncated series expansions. The resulting velocity field is expressed in terms of both the vertical and the horizontal velocity components at the still-water datum. The result is a system of six coupled equations with the unknowns being the surface elevation, the horizontal gradient of the velocity potential at the free surface, and the horizontal and vertical velocities at the free surface and at the still-water level. As a result the AMS99 formulation allows an accurate description of dispersive nonlinear waves up to $kh \approx 6$.

One problem, which AMS99 did not resolve, is to provide an accurate vertical distribution of the velocity field. This turns out to be an even more severe restriction to conventional Boussinesq formulations and most existing formulations can only produce a reasonable velocity profile for $kh \leqslant 0.5$. Two exceptions are the formulations of Nwogu (1993) and Gobbi *et al.* (2000). Nwogu (1993) expanded the velocity field from an arbitrary z-level, which was taken to be approximately mid-depth. The objective of Nwogu was not to improve the velocity profile but the linear dispersion. Nevertheless, the profile obtained from his lower-order formulation is accurate up to $kh \approx 1.5$ and can be shown to converge up to $kh = 3.5$ (if higher-order terms are included). Recently, Gobbi *et al.* (2000) presented a higher-order formulation based on a linear combination of the velocities at two arbitrary z-levels. The linear velocity profile obtained from their method is applicable up to $kh \approx 4$, while their dispersion relation is applicable up to $kh \approx 6$.

In the present work, we generalize the procedure of AMS99 and expand the Laplace solution from an arbitrary z-level rather than from the still-water datum. The arbitrary z-level is determined by minimizing the depth-integrated error of the linear velocity profile. However, the possibility of minimizing the error of the linear dispersion relation is also investigated. In § 2, we present the theoretical formulation involving exact boundary conditions on the free surface and a truncated series expansion solution to the Laplace equation. This expansion, which involves fifth-derivative operators, is manipulated using Padé approximants in order to achieve the best possible accuracy relative to the number of terms included. In § 3, we perform a linear analysis to quantify the accuracy of dispersion, shoaling and velocity profiles. In § 4, we extend the perturbation analysis to weakly nonlinear waves and determine second- and third-order transfer functions for regular waves, including amplitude-dispersion and second-order transfer functions for bichromatic waves. The numerical solution algorithm for two-dimensional problems is presented in § 5, while § 6 presents different applications of the model, including phenomena such as the propagation of solitary waves, their impact on vertical walls, Benjamin–Feir-type instabilities in deep water involving recurrence or frequency downshift, and nonlinear shoaling of regular waves up to the point of breaking. Concluding remarks are made in § 7.

2. The theoretical formulation

2.1. *The exact solution in terms of infinite series expansions*

Consider the irrotational flow of an incompressible inviscid fluid with a free surface. A Cartesian coordinate system is adopted, with the x-axis and y-axis located on the still-water plane and with the z-axis pointing vertically upwards. The fluid domain is bounded by the sea bed at $z = -h(x, y)$ and the free surface at $z = \eta(x, y, t)$. Following Zakharov (1968), Witting (1984), Dommermuth & Yue (1987) and AMS99, we express the kinematic and dynamic surface conditions in terms of velocity variables defined

directly on the free surface, i.e.

$$\eta_t - \tilde{w} + \nabla\eta \cdot \tilde{\boldsymbol{u}} = 0, \tag{1}$$

$$\tilde{\boldsymbol{V}}_t + g\nabla\eta + \nabla\left(\frac{\tilde{\boldsymbol{V}}\cdot\tilde{\boldsymbol{V}}}{2} - \frac{\tilde{w}^2}{2}(1+\nabla\eta\cdot\nabla\eta)\right) = 0, \tag{2}$$

where

$$\tilde{\boldsymbol{V}} \equiv \tilde{\boldsymbol{u}} + \tilde{w}\nabla\eta. \tag{3}$$

Here $\tilde{\boldsymbol{u}}$ is the horizontal velocity vector and $\tilde{w}$ is the vertical velocity component, both defined directly on the free surface. Furthermore, ∇ is the horizontal gradient operator defined by

$$\nabla \equiv \left(\frac{\partial}{\partial x}, \frac{\partial}{\partial y}\right).$$

For details of the derivation of (1)–(3) the reader is referred to AMS99.

Note that (1)–(3) define the fully nonlinear time-stepping problem. However, to establish a connection between the vertical and horizontal velocity variables at the free surface, we need to solve the Laplace equation in the interior domain. Following Madsen & Schäffer (1998, 1999) and AMS99, we first express an exact solution to the Laplace equation in terms of

$$\boldsymbol{u}(x,y,z,t) = \cos(z\nabla)\boldsymbol{u}_0 + \sin(z\nabla)w_0, \tag{4a}$$

$$w(x,y,z,t) = \cos(z\nabla)w_0 - \sin(z\nabla)\boldsymbol{u}_0, \tag{4b}$$

where $\boldsymbol{u}_0, w_0$ are the velocity components at the still-water level $z = 0$, while the cos- and sin-operators are infinite Taylor series operators defined by

$$\cos(\lambda\nabla) \equiv \sum_{n=0}^{\infty}(-1)^n\frac{\lambda^{2n}}{(2n)!}\nabla^{2n}, \quad \sin(\lambda\nabla) \equiv \sum_{n=0}^{\infty}(-1)^n\frac{\lambda^{2n+1}}{(2n+1)!}\nabla^{2n+1}, \tag{5}$$

with λ being the expansion coordinate of the Taylor series. Throughout this paper the interpretation of the powers of ∇ depends on whether this operator is acting on a scalar or a vector and in this context the following set of rules should be obeyed (see Madsen & Schäffer 1999, Chap. 5)

$$\nabla^{2n}\boldsymbol{u}_0 \equiv \nabla(\nabla^{2n-2}(\nabla\cdot\boldsymbol{u}_0)), \quad \nabla^{2n+1}\boldsymbol{u}_0 \equiv \nabla^{2n}(\nabla\cdot\boldsymbol{u}_0),$$
$$\nabla^{2n}w_0 \equiv \nabla^{2n}w_0, \qquad\qquad \nabla^{2n+1}w_0 \equiv \nabla(\nabla^{2n}w_0).$$

Note that (4*a*, *b*) define the velocity profile in the entire water column ranging from the free surface ($z = \eta$) to the sea bed ($z = -h$) expressed in terms of the velocity variables at $z = 0$. The remaining condition necessary to close the system of equations is the kinematic bottom condition,

$$w_b + \nabla h\cdot\boldsymbol{u}_b = 0, \tag{6}$$

where $\boldsymbol{u}_b, w_b$ are the velocity components at the sea bottom.

As shown by AMS99, a linear analysis of the system of equations (1), (2), (3) and (6) combined with (4*a*, *b*) and (5) recovers the exact linear dispersion relation and the exact linear shoaling gradient. On the other hand, it is necessary to truncate (5) in order to establish finite-order equations, which can be solved numerically, and this process will generally reduce the accuracy of the imbedded linear and nonlinear properties of the equations. AMS99 included the first three terms in (5) and found that linear and nonlinear properties were accurate up to a wavenumber times water depth, kh of 6. This was a major step forward compared to previous Boussinesq

formulations. Unfortunately, the truncated vertical variation of the velocity profile ($4a, b$) is not very accurate, and it quickly deteriorates below the still-water datum for kh higher than $\pi/2$.

In order to relax this limitation, we generalize ($4a, b$) in the following. The first step is to introduce $\hat{u}, \hat{w}$ which are velocity components taken at an arbitrary level $z = \hat{z}$, where $\hat{z}$ is assumed to be a constant fraction (σ) of the still-water depth and thus a function of x and y, except on a horizontal bottom. This generalization of the formulation by AMS99 is inspired by Nwogu (1993), who was the first to formulate truncated Boussinesq equations in terms of the horizontal velocity vector defined at an arbitrary z-level. However, while Nwogu used the free parameter σ to optimize linear dispersion, the main objective of our formulation is to improve the vertical profile of the velocity field. We shall return to this issue in § 3.

From ($4a, b$) we find the relations,

$$\hat{\boldsymbol{u}} = \cos(\hat{z}\nabla)\boldsymbol{u}_0 + \sin(\hat{z}\nabla)w_0, \tag{7a}$$

$$\hat{w} = \cos(\hat{z}\nabla)w_0 - \sin(\hat{z}\nabla)\boldsymbol{u}_0. \tag{7b}$$

In order to invert ($7a, b$) and determine $\boldsymbol{u}_0, w_0$ in terms of $\hat{\boldsymbol{u}}, \hat{w}$, we insert (5) in ($7a, b$) and use successive approximations assuming high-derivative terms to be smaller than low-derivative terms. The inversion process involves higher derivatives of $\hat{z}$ and in the following we shall include only terms which are $O(\nabla\hat{z})$ corresponding to a mild-slope approximation. Finally, we insert the inverted expressions for $\boldsymbol{u}_0, w_0$ in ($4a, b$) and derive the following mild-slope expression for the velocity field:

$$\boldsymbol{u}(x, y, z, t) = \cos((z - \hat{z})\nabla)\hat{\boldsymbol{u}} + \sin((z - \hat{z})\nabla)\hat{w} + \Gamma_u\nabla\hat{z}, \tag{8a}$$

$$w(x, y, z, t) = \cos((z - \hat{z})\nabla)\hat{w} - \sin((z - \hat{z})\nabla)\hat{\boldsymbol{u}} + \boldsymbol{\Gamma}_w \cdot \nabla\hat{z}, \tag{8b}$$

where

$$\Gamma_u \equiv (z - \hat{z})(\cos((z - \hat{z})\nabla)\nabla \cdot \hat{\boldsymbol{u}} + \sin((z - \hat{z})\nabla)\nabla\hat{w}), \tag{8c}$$

$$\boldsymbol{\Gamma}_w \equiv (z - \hat{z})(\cos((z - \hat{z})\nabla)\nabla\hat{w} - \sin((z - \hat{z})\nabla)\nabla \cdot \hat{\boldsymbol{u}}). \tag{8d}$$

This completes the formulation of the un-truncated system of equations, which consists of (1), (2), (3), (6) and ($8a$–d) expressed in terms of the unknowns $\eta, \hat{\boldsymbol{u}}$ and $\hat{w}$. A linear analysis of this un-truncated system can be found in Madsen, Bingham & Schäffer (2002), and this recovers the exact linear velocity profile, the linear dispersion relation and the linear shoaling gradient. An interesting conclusion from this analysis is that the $\nabla\hat{z}$ terms in ($8a, b$) have no impact on the imbedded linear shoaling properties. The $\nabla\hat{z}$ terms do influence the velocity profile but this is a local influence of minor importance if the bottom slope is mild. Consequently, we shall ignore the $\Gamma_u, \boldsymbol{\Gamma}_w$ terms in the present work.

2.2. *Finite series expansions involving Padé approximations*

We now consider various schemes for truncating the above expansions in such a way as to achieve the best possible accuracy with a given number of terms. As a starting point, we follow AMS99 and include the first three terms in both the cos- and the sin-series defined in (5). This leads to the approximations

$$\cos(\lambda\nabla) = 1 - \frac{\lambda^2\nabla^2}{2} + \frac{\lambda^4\nabla^4}{24} + O(\lambda^6\nabla^6), \tag{9a}$$

$$\sin(\lambda\nabla) = \lambda\nabla - \frac{\lambda^3\nabla^3}{6} + \frac{\lambda^5\nabla^5}{120} + O(\lambda^7\nabla^7). \tag{9b}$$

By inserting $(9a,b)$ in $(8a,b)$ and analysing the resulting velocity profile, it can be shown that the accuracy will increase significantly by choosing $\hat{z} = -0.5h$, rather than the $\hat{z} = 0$ used by AMS99 (for details see Madsen *et al.* 2002). On the other hand, it turns out that an even better accuracy can be achieved by the procedure presented in the following.

First, we expand the physical velocity variables $\hat{\boldsymbol{u}}, \hat{w}$ in terms of utility velocity variables $\hat{\boldsymbol{u}}^*, \hat{w}^*$ using the connection

$$\hat{\boldsymbol{u}} \equiv L(\hat{z}\nabla)\hat{\boldsymbol{u}}^*, \quad \hat{w} \equiv L(\hat{z}\nabla)\hat{w}^*, \tag{10}$$

where L is a linear operator to be determined. We note that there is some similarity between this approach and the previous ideas of Schäffer & Madsen (1995) and Gobbi *et al.* (2000) who also used generalized velocity variables rather than physical velocity variables. However, the choice of the L-operator is very important in this process, as shown below. We insert (10) in $(8a,b)$ while neglecting the $\Gamma_u, \boldsymbol{\Gamma}_w$ terms and obtain

$$\boldsymbol{u}(x,y,z,t) = \cos((z-\hat{z})\nabla)L(\hat{z}\nabla)\hat{\boldsymbol{u}}^* + \sin((z-\hat{z})\nabla)L(\hat{z}\nabla)\hat{w}^*, \tag{11a}$$

$$w(x,y,z,t) = \cos((z-\hat{z})\nabla)L(\hat{z}\nabla)\hat{w}^* - \sin((z-\hat{z})\nabla)L(\hat{z}\nabla)\hat{\boldsymbol{u}}^*. \tag{11b}$$

Note that at $z = 0$, $(11a,b)$ simplifies to

$$\boldsymbol{u}_0 = \cos(\hat{z}\nabla)L(\hat{z}\nabla)\hat{\boldsymbol{u}}^* - \sin(\hat{z}\nabla)L(\hat{z}\nabla)\hat{w}^*, \tag{12a}$$

$$w_0 = \cos(\hat{z}\nabla)L(\hat{z}\nabla)\hat{w}^* + \sin(\hat{z}\nabla)L(\hat{z}\nabla)\hat{\boldsymbol{u}}^*, \tag{12b}$$

and this now defines the connection between the still-water velocities $\boldsymbol{u}_0, w_0$ and the utility velocities $\hat{\boldsymbol{u}}^*, \hat{w}^*$.

Our objective is to choose L in such a way that the accuracy of $(12a,b)$ is improved relative to the Taylor expansion given by $(9a,b)$. It is indeed possible to achieve a much higher order of accuracy without increasing the order of the derivatives if the L operator is chosen to introduce Padé approximants in the truncated equations. With this purpose we follow the general procedure described by Madsen & Schäffer (1998) and AMS99 and define the L operator by

$$L(\lambda\nabla) \equiv 1 + \sum_{n=1}^{N} \delta_{2n}\lambda^{2n}\nabla^{2n}, \tag{13a}$$

where δ_{2n} are arbitrary coefficients. To determine these coefficients, we truncate the infinite cos- and sin-operators at $2N$ and $2N+1$, respectively, multiply $(13a)$ by each of the series, and require that all constant-depth terms with powers of $N+2$ to $2N+1$ vanish. For constant λ and for the case of $N = 4$, this procedure yields

$$\delta_2 = \frac{1}{18}, \quad \delta_4 = \frac{1}{504}, \quad \delta_6 = \frac{1}{15120}, \quad \delta_8 = \frac{1}{362880}, \tag{13b}$$

and consequently we obtain

$$\cos(\lambda\nabla)L(\lambda\nabla) = 1 - \frac{4}{9}(\lambda\nabla)^2 + \frac{1}{63}(\lambda\nabla)^4 + O(\lambda^{10}\nabla^{10}), \tag{14a}$$

$$\sin(\lambda\nabla)L(\lambda\nabla) = \lambda\nabla - \frac{1}{9}(\lambda\nabla)^3 + \frac{1}{945}(\lambda\nabla)^5 + O(\lambda^{11}\nabla^{11}). \tag{14b}$$

Note that now the accuracy has become twice the order of the terms included, which is a typical property of Padé approximants, and with this procedure the

formal accuracy of (12a,b) has increased from $O(\nabla^5)$ to $O(\nabla^9)$. Unfortunately, this achievement requires that the L-, cos- and sin-operators have the same argument and this is only the case at $z = 0$. Hence, in general the velocity profile given by (11a,b) is still $O(\nabla^5)$. Nevertheless, the analysis in § 3 will demonstrate that in practice the profile of (11a,b) is much more accurate than the one obtained from (8a,b) and in addition this improvement spills over to the imbedded linear and nonlinear properties.

Now the resulting velocity field is determined by inserting (13a,b) in (11a,b) while ignoring spatial derivatives higher than fifth order. This leads to

$$\boldsymbol{u}(x,y,z,t) = (1-\alpha_2\nabla^2+\alpha_4\nabla^4)\hat{\boldsymbol{u}}^* + ((z-\hat{z})\nabla-\beta_3\nabla^3+\beta_5\nabla^5)\hat{w}^* + \Lambda_u\nabla\hat{z}, \quad (15a)$$

$$w(x,y,z,t) = (1-\alpha_2\nabla^2+\alpha_4\nabla^4)\hat{w}^* - ((z-\hat{z})\nabla-\beta_3\nabla^3+\beta_5\nabla^5)\hat{\boldsymbol{u}}^* + \boldsymbol{\Lambda}_w\cdot\nabla\hat{z}, \quad (15b)$$

where

$$\alpha_2 \equiv \frac{(z-\hat{z})^2}{2} - \frac{\hat{z}^2}{18}, \quad \alpha_4 \equiv \frac{(z-\hat{z})^4}{24} - \frac{\hat{z}^2(z-\hat{z})^2}{36} + \frac{\hat{z}^4}{504}, \quad (16a)$$

$$\beta_3 \equiv \frac{(z-\hat{z})^3}{6} - \frac{\hat{z}^2(z-\hat{z})}{18}, \quad \beta_5 \equiv \frac{(z-\hat{z})^5}{120} - \frac{\hat{z}^2(z-\hat{z})^3}{108} + \frac{\hat{z}^4(z-\hat{z})}{504}. \quad (16b)$$

We note that the $\Lambda_u, \boldsymbol{\Lambda}_w$ terms proportional to gradients of $\hat{z}$ arise from the successive use of the L-, cos- and sin-operators. These terms do influence the accuracy of linear shoaling, in contrast to the $\Gamma_u, \boldsymbol{\Gamma}_w$ terms in (8a,b). Their impact will be analysed and discussed in § 3, where we conclude that these terms can eventually be ignored in the final model setup.

Although nothing prohibits the use of (15a,b) and (16a,b) from the sea bed to the instantaneous free surface, it turns out to be more accurate to restrict its use to the region from the sea bed to the still-water datum. From the still-water datum to the free surface we apply (8a,b) with the Taylor approximations (9a,b), i.e.

$$\boldsymbol{u}(x,y,z,t) = \left(1-\frac{1}{2}z^2\nabla^2+\frac{1}{24}z^4\nabla^4\right)\boldsymbol{u}_0 + \left(z\nabla-\frac{1}{6}z^3\nabla^3+\frac{1}{120}z^5\nabla^5\right)w_0, \quad (17a)$$

$$w(x,y,z,t) = \left(1-\frac{1}{2}z^2\nabla^2+\frac{1}{24}z^4\nabla^4\right)w_0 - \left(z\nabla-\frac{1}{6}z^3\nabla^3+\frac{1}{120}z^5\nabla^5\right)\boldsymbol{u}_0. \quad (17b)$$

The advantage of combining (15a,b) with (17a,b) versus the option of applying (15a,b) everywhere will be demonstrated in § 4.2 for the case of highly nonlinear steady waves.

2.3. *The kinematic condition at the sea bed*

The remaining boundary condition is the kinematic condition at the sea bed. We insert (11a,b) in (6) and multiply the resulting equation with a new linear operator M to obtain

$$M\cos((h+\hat{z})\nabla)L(\hat{z}\nabla)\hat{w}^* + M\sin((h+\hat{z})\nabla)L(\hat{z}\nabla)\hat{\boldsymbol{u}}^* + M\nabla h\cdot(\cos((h+\hat{z})\nabla)L(\hat{z}\nabla)\hat{\boldsymbol{u}}^* - \sin((h+\hat{z})\nabla)L(\hat{z}\nabla)\hat{w}^*) = 0, \quad (18)$$

where M will be chosen to optimize the accuracy of linear dispersion.

Constant water depth On a constant depth (18) simplifies to

$$M\cos((h+\hat{z})\nabla)L(\hat{z}\nabla)\hat{w}^* + M\sin((h+\hat{z})\nabla)L(\hat{z}\nabla)\hat{\boldsymbol{u}}^* = 0, \quad (19)$$

and this determines a connection between $\hat{w}^*$ and $\hat{\boldsymbol{u}}^*$, which is crucial for the accuracy of the linear dispersion relation. As discussed above, the doubling of the accuracy of

(14a,b) relative to (9a,b) requires that the L-, cos- and sin-operators have the same argument, and this is not the case in (19). However, we can achieve this by requiring that the M-operator satisfies the conditions

$$M\cos((h+\hat{z})\nabla)L(\hat{z}\nabla) = \cos((h+\hat{z})\nabla)L((h+\hat{z})\nabla), \tag{20a}$$

$$M\sin((h+\hat{z})\nabla)L(\hat{z}\nabla) = \sin((h+\hat{z})\nabla)L((h+\hat{z})\nabla). \tag{20b}$$

On a constant depth, the solution to (20a,b) is

$$M \equiv \frac{L((h+\hat{z})\nabla)}{L(\hat{z}\nabla)}, \tag{21}$$

where L is given by (13a,b). This expression is not very attractive as it involves a rational function of operators, and in practice we approximate M by the Taylor series expansion of (21). Using this operator on (19) now leads to

$$\left(1-\frac{4}{9}\lambda^2\nabla^2+\frac{1}{63}\lambda^4\nabla^4\right)\hat{w}^* + \left(\lambda\nabla-\frac{1}{9}\lambda^3\nabla^3+\frac{1}{945}\lambda^5\nabla^5\right)\hat{\boldsymbol{u}}^* = O(\lambda^{10}\nabla^{10}), \tag{22a}$$

with $\lambda = (h+\hat{z})$.

Mildly sloping bottom On an uneven bottom, slope terms involving higher derivatives of the water depth will appear due to the successive use of L-, cos-/sin- and M-operators. In this process we again assume a mildly sloping bottom and include only first derivatives of h. By truncating the slope terms after the fifth derivatives we obtain

$$\left(1-\frac{4}{9}\lambda^2\nabla^2+\frac{1}{63}\lambda^4\nabla^4\right)\hat{w}^* + \left(\lambda\nabla-\frac{1}{9}\lambda^3\nabla^3+\frac{1}{945}\lambda^5\nabla^5\right)\hat{\boldsymbol{u}}^* + \nabla h\cdot(1-c_2\lambda^2\nabla^2+c_4\lambda^4\nabla^4)\hat{\boldsymbol{u}}^* - \nabla h\cdot(\lambda\nabla-s_3\lambda^3\nabla^3+s_5\lambda^5\nabla^5)\hat{w}^* = 0, \tag{22b}$$

where $\lambda = (h+\hat{z})$, and where c_2, c_4, s_3, s_5 are coefficients depending on the choice of $\hat{z}$. A further discussion of these coefficients and their determination is given in § 3.

3. Linear Fourier analysis of dispersion, shoaling and velocity

Linear dispersion and linear shoaling are some of the fundamental quantities imbedded in the governing equations for water wave propagation over varying bathymetry. In this section, we analyse the new Boussinesq-type formulation and compare to the well-known results from linear theory.

The following Fourier analysis proceeds from equations (1), (2), (3), (22b) and (15a,b). First, linearization gives $\tilde{\boldsymbol{V}} = \tilde{\boldsymbol{u}} = \boldsymbol{u}_0$ and $\tilde{w} = w_0$, while (1) and (2) simplify to

$$\boldsymbol{u}_{0t} + g\nabla\eta = 0, \quad \eta_t - w_0 = 0. \tag{23}$$

Restricting the analysis to one horizontal dimension, we look for solutions of the form

$$\eta(x,t) = A(x)\,\mathrm{e}^{\mathrm{i}\theta}, \quad \theta \equiv \omega t - \int k(x)\,\mathrm{d}x, \tag{24a}$$

$$\hat{u}^*(x,t) = (B_1(x) + \mathrm{i}h_x B_2(x))\,\mathrm{e}^{\mathrm{i}\theta}, \tag{24b}$$

$$\hat{w}^*(x,t) = \mathrm{i}(C_1(x) + \mathrm{i}h_x C_2(x))\,\mathrm{e}^{\mathrm{i}\theta}, \tag{24c}$$

where i is the imaginary unit, k the wavenumber, ω the cyclic frequency and h_x

the bottom slope, assumed to be small. We note that A, B_1, B_2, C_1 and C_2 are real functions with a slow spatial variation. Due to the sloping bottom, the horizontal velocity variable will only be in phase with the surface elevation to the lowest order, which is why the B_2 and C_2 contributions are necessary. When evaluating higher derivatives of the harmonic functions, only constant-depth and mild-slope terms are retained (i.e. zeroth and first derivatives of the slowly varying quantities).

The lowest-order problem neglects all derivatives of the slowly varying quantities and leads to three homogeneous equations in A, B_1, C_1. We express B_1, C_1 in terms of A, and require that the determinant is zero to obtain non-trivial solutions. This leads to

$$B_1 = \frac{A}{\omega}\left(\frac{\omega^2 \operatorname{sh}(k\hat{z}) + gk \operatorname{ch}(k\hat{z})}{\operatorname{ch}^2(k\hat{z}) - \operatorname{sh}^2(k\hat{z})}\right), \tag{25a}$$

$$C_1 = \frac{A}{\omega}\left(\frac{\omega^2 \operatorname{ch}(k\hat{z}) + gk \operatorname{sh}(k\hat{z})}{\operatorname{ch}^2(k\hat{z}) - \operatorname{sh}^2(k\hat{z})}\right), \tag{25b}$$

and the dispersion relation

$$\frac{\omega^2}{ghk^2} = \frac{1}{kh}\left(\frac{\operatorname{sh}(k(h+\hat{z}))\operatorname{ch}(k\hat{z}) - \operatorname{ch}(k(h+\hat{z}))\operatorname{sh}(k\hat{z})}{\operatorname{ch}(k(h+\hat{z}))\operatorname{ch}(k\hat{z}) - \operatorname{sh}(k(h+\hat{z}))\operatorname{sh}(k\hat{z})}\right), \tag{25c}$$

where the ch and sh functions are defined by

$$\operatorname{ch}(\lambda) \equiv \left(1 + \frac{4}{9}\lambda^2 + \frac{1}{63}\lambda^4\right), \quad \operatorname{sh}(\lambda) \equiv \left(\lambda + \frac{1}{9}\lambda^3 + \frac{1}{945}\lambda^5\right). \tag{26}$$

Note that if infinite operators are applied, the ch and sh functions should be replaced by the cosh- and sinh-functions, by which the denominators in (25a, b) go to unity and (25c) simplifies to

$$\frac{\omega^2}{ghk^2} = \frac{1}{kh}\left(\frac{\sinh(k(h+\hat{z}) - k\hat{z})}{\cosh(k(h+\hat{z}) - k\hat{z})}\right) = \frac{\tanh(kh)}{kh}, \tag{27}$$

recovering the exact linear dispersion relation.

3.1. *The accuracy of the linear dispersion relation*

For the special case of $\hat{z} = 0$ (considered by AMS99), the dispersion relation (25c) simplifies to

$$\frac{c^2}{gh} \equiv \frac{\omega^2}{ghk^2} = \frac{1 + \frac{1}{9}k^2h^2 + \frac{1}{945}k^4h^4}{1 + \frac{4}{9}k^2h^2 + \frac{1}{63}k^4h^4}, \quad \hat{z} = 0,$$

which is the Padé [4, 4] approximation to the target solution (27). For arbitrary $\hat{z} = \sigma h$, (25c) will contain powers of kh up to 8 in the numerator and 10 in the denominator. We check the formal order of accuracy by making a series expansion of this expression from $kh = 0$ and this leads to errors relative to fully dispersive theory at $k^{10}h^{10}$ for arbitrary σ. In reality, the applicability of (25c) depends on the choice of σ. One option is to use σ to minimize the error of (25c), i.e.

$$\frac{1}{\kappa_0}\int_0^{\kappa_0}\left(\frac{c - c_S}{c_S}\right)^2 \mathrm{d}kh,$$

where c_S is determined from (27). With $\kappa_0 = 25$ this leads to $\sigma = -0.2028$, which is approximated by $\sigma = -0.2$.

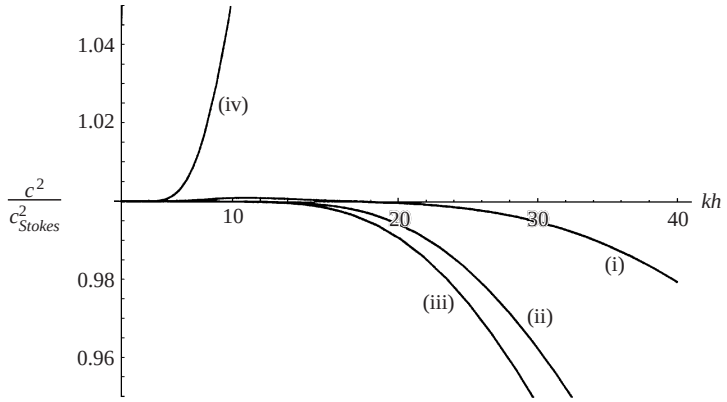

FIGURE 1. The accuracy of the square of the phase celerity using (25*c*) and (26). (i) $\sigma = -0.2$; (ii) $\sigma = -0.5$; (iii) Padé [8, 10] expansion of target solution; (iv) $\sigma = 0$, Padé [4, 4].

The celerity is shown in figure 1 for $\sigma = -0.2$ (optimal celerity) and for $\sigma = -0.5$ (optimal velocity distribution to be discussed below). In both cases the accuracy is significantly better than what was achieved with the Padé [4, 4] approximation (AMS99) and at least as accurate as the Padé [8, 10] approximation. A 2% error is reached at $kh = 25$ for $\sigma = -0.5$ and at $kh = 40$ for $\sigma = -0.2$.

3.2. *The accuracy of the velocity field on a constant depth*

The linear velocity field is determined by inserting (24*b*, *c*), (25*a*–*c*) and (26) into (15*a*, *b*). To quantify the accuracy of the vertical variation of the horizontal velocity component, we introduce the measures

$$F_{u1}(\sigma, kh) \equiv \sqrt{\frac{1}{h}\int_{-h}^{0}\left(\frac{u(z) - u_S(z)}{u_S(0)}\right)^2 \mathrm{d}z}, \quad F_{u2}(\sigma) \equiv \sqrt{\frac{1}{\kappa_0}\int_0^{\kappa_0} F_{u1}^2 \,\mathrm{d}kh}, \tag{28}$$

where u_S denotes the target velocity according to Stokes linear theory. Similar measures F_{w1} and F_{w2} apply for the vertical velocity component. Figure 2(*a*) shows the variation of F_{u1} as a function of σ for discrete values of kh in the interval from 2 to 12. All the curves show a minimum error for $\sigma \approx -0.5$ for which the depth-integrated error is limited to less than 2% for kh as large as 12. We calculate F_{u2} as defined by (28) and minimize this function to determine the optimal value of σ. With $\kappa_0 = 10$, this leads to $\sigma = -0.48921$ for which $(F_{u2}, F_{w2}) = (0.0042, 0.0043)$. For simplicity we choose $\sigma = -0.5$ for which $(F_{u2}, F_{w2}) = (0.0045, 0.0046)$.

Figure 2(*b*) shows F_{u1} and F_{w1} as functions of kh for $\sigma = -0.5$ and we notice that it provides depth-integrated errors of 1% for $kh \approx 9.5$ and 2% for $kh \approx 12$. For reference, figure 2(*b*) also shows the performance of the velocity profile determined from (8*a*, *b*) with (9*a*, *b*), e.g. the profile obtained without invoking the *L*- and *M*-operators. Also in this case the optimal choice of σ turns out to be $\sigma \approx -0.5$, but clearly the applicability of this profile is much more restricted.

Finally, it should be emphasized, that the choice of $\sigma = -0.2$ (optimum celerity) leads to a relatively poor velocity profile according to figure 2(*a*). The solution to this problem is to replace (16*a*, *b*) with optimized velocity coefficients. Such a procedure is described in Madsen *et al.* (2002).

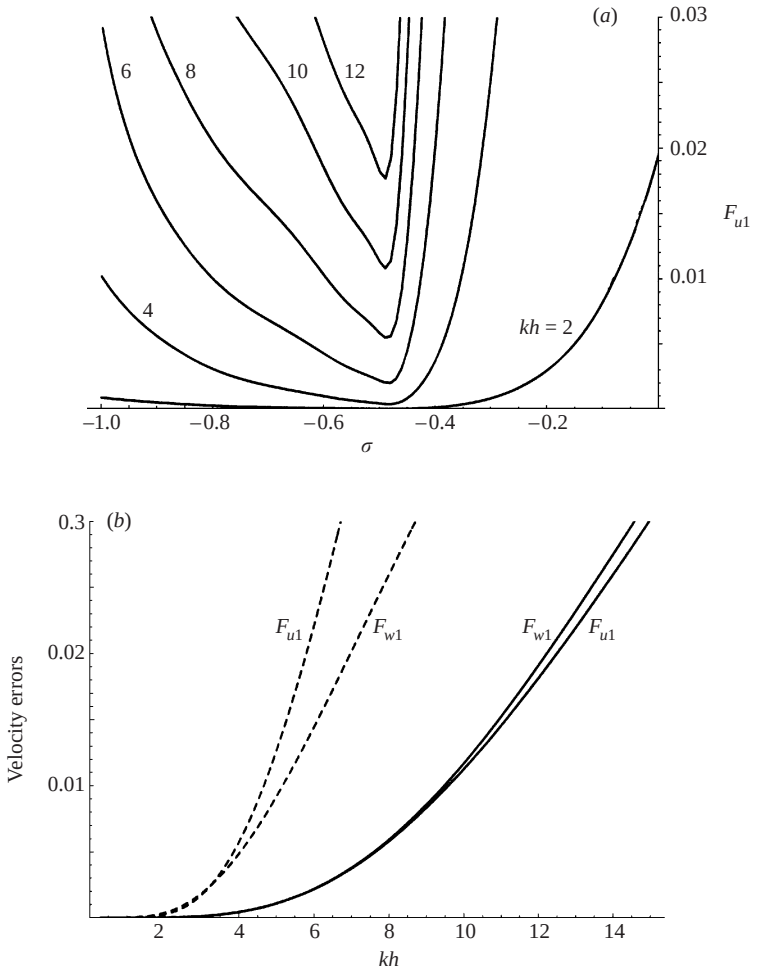

FIGURE 2. (*a*) The depth-averaged error in the horizontal velocity component shown as a function of σ for discrete values of kh. Velocity profile based on (15*a*, *b*) and (16*a*, *b*). (*b*) The depth-averaged error in the horizontal and vertical velocity components. Full line: (15*a*, *b*) and (16*a*, *b*), dashed line: (8*a*, *b*) and (9*a*, *b*); $\sigma = -0.5$.

3.3. *The accuracy of linear shoaling*

We continue the linear analysis to the next order and collect terms proportional to the first derivatives of the variables. This leads to three inhomogeneous equations with the unknowns A_x, B_2, C_2 expressed in terms of k_x, h_x and the first derivatives of B_1, C_1. The latter derivatives can be expressed in terms of A_x, k_x, h_x by differentiation of (25*a*, *b*), while differentiation of the dispersion relation (25*c*) yields k_x in terms of h_x. As a result, we can determine A_x, B_2, C_2, and finally the linear shoaling gradient γ is determined by the definition

$$\frac{A_x}{A} = -\gamma \frac{h_x}{h}. \tag{29}$$

The result is a function of σ and it can be compared to the target solution, which was derived by Madsen & Sørensen (1993) using energy flux conservation combined

with Stokes linear theory,

$$\gamma_S = \frac{2kh\sinh(2kh) + 2k^2h^2(1-\cosh(2kh))}{(2kh+\sinh(2kh))^2}. \tag{30}$$

We check the formal accuracy of the resulting shoaling gradient by comparing the Taylor series expansions from $kh = 0$.

First, we consider the case where Λ_u, Λ_w in (15a, b) as well as c_2, c_4, s_3, s_5 in (22b) are determined from a consistent successive use of the L-, cos / sin- and M-operators. Including up to fifth-derivative slope terms leads to a formal error in the shoaling gradient of $O(k^6h^6)$. This is disappointing, but the error can be reduced to $O(k^{10}h^{10})$ if we also include the sixth-derivative slope terms in Λ_u, Λ_w in (22b).

A much more attractive approach is, however, to neglect the Λ_u, Λ_w-terms completely, while considering the c_2, c_4, s_3, s_5-coefficients in (22b) as free parameters. Formally, this corresponds to replacing the M-operator with $M + N\nabla h$, where N contains a number of free parameters which can be adjusted to improve the accuracy of the slope terms. With this approach we could use c_2, c_4, s_3, s_5 to cancel the formal errors of the shoaling gradient up to $O(k^{10}h^{10})$, but in fact we can do better than that by optimizing either the shoaling gradient or the accumulated shoaling. Chen & Liu (1995) advocated the latter choice, because relative errors in the shoaling gradient are far more critical in shallow water than in deep water. Hence they suggested optimizing

$$\frac{A}{A_S} = \exp\left(-\int_0^{\kappa_0} \frac{\gamma - \gamma_S}{k_0 h}\mathrm{d}k_0 h\right), \tag{31}$$

where A/A_S is the accumulated shoaling amplitude over the target amplitude and k_0 is the linear deep-water wavenumber. This integration involves the relevant dispersion relations to connect the local wavenumbers to the fixed deep-water wavenumber.

We have attempted to optimize (31), but have not succeeded due to the complexity of terms involved. Instead, we optimize

$$F_3(c_2, c_4, s_3, s_5) \equiv \int_0^{\kappa_0} \frac{1}{kh}(\gamma - \gamma_S)^2\,\mathrm{d}kh, \tag{32}$$

where the division by kh will emphasize the importance of keeping errors to a minimum in shallow water.

With $\kappa_0 = 30$ this procedure leads to
$\sigma = -0.5$:

$$c_2 = 0.357739, \quad c_4 = 0.00663819, \quad s_3 = 0.0753019, \quad s_5 = -6.31532 \times 10^{-5}.$$

$\sigma = -0.2$:

$$c_2 = 0.369651, \quad c_4 = 0.00510326, \quad s_3 = 0.0656786, \quad s_5 = -1.84353 \times 10^{-4}.$$

As a check, we compute (31) for the optimized coefficients and find that the relative errors of the accumulated shoaling amplitudes are less than 0.5% for $0 < kh < 30$.

4. Analysis of nonlinear properties

4.1. *Transfer functions for subharmonics and superharmonics*

In order to analyse the accuracy of second-order subharmonic and superharmonic interactions, we consider on a constant depth the forcing due to a simple first-order wave group made up of just two frequencies ω_n and ω_m. At second order,

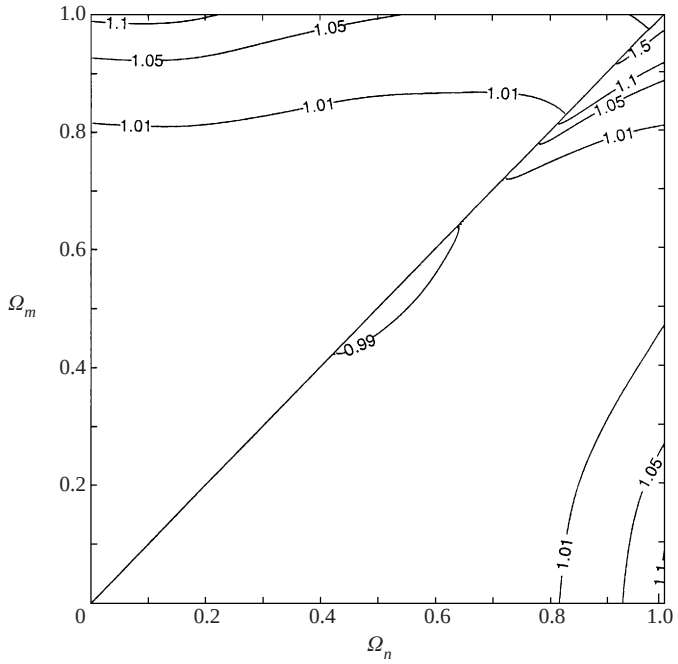

FIGURE 3. The accuracy of the second order transfer functions, G_η/G^{Stokes}. Superharmonic G_η^+ shown above the diagonal; subharmonic $-G_\eta^-$ shown below it. Computed with $\sigma = -0.2$. Note that $\Omega = 1.0$ corresponds to $kh = 39.5$.

quadratic nonlinearities will force a wave train consisting of four contributions: one subharmonic at $\omega_p = \omega_n - \omega_m$, and three superharmonics at $\omega_p = \omega_n + \omega_m$, $\omega_p = 2\omega_n$ and $\omega_p = 2\omega_m$ with corresponding wavenumbers determined by $k_p = k_n - k_m$, $k_p = k_n + k_m$, $k_p = 2k_n$ and $k_p = 2k_m$. These waves are bound or phase-locked to the first-order wave train and (ω_p, k_p) does not satisfy the linear dispersion relation. $G_\eta^\pm$ denotes the second-order surface elevation transfer function, where the subharmonic/superharmonic contributions are found by using the lower/upper signs. The reference solution $G_\eta^{\pm\text{Stokes}}$, determined directly from the original nonlinear boundary value problem for the Laplace equation, was given by e.g. Ottesen-Hansen (1978) for the subharmonics and Sand & Mansard (1986) for the superharmonics (see also Dean & Sharma 1981 and Schäffer 1996).

Figure 3 shows the variation of the ratio of $G_\eta^\pm$ to $G_\eta^{\pm\text{Stokes}}$ as a function of the non-dimensional interacting frequencies Ω_n and Ω_m, where

$$\Omega_n = \frac{\omega_n}{2\pi}\sqrt{\frac{h}{g}}, \quad \Omega_m = \frac{\omega_m}{2\pi}\sqrt{\frac{h}{g}}.$$

We note that the corresponding wavenumbers are determined by solving the dispersion relation which leads to (Ω, kh): (0.2, 1.7), (0.4, 6.3), (0.6, 14.2), (0.8, 25.2), (1.0, 39.5). The portion above the diagonal in figure 3 represents the superharmonic transfer from ω_n and ω_m to $\omega_p = \omega_n + \omega_m$, while the lower portion represents the subharmonic transfer from ω_n and ω_m to $\omega_p = \omega_n - \omega_m$. The diagonal line on which ω_n equals ω_m represents the self–self interaction. With $\sigma = -0.2$ the transfer functions are seen to have an outstanding accuracy with errors less than 1% up to $(\Omega, kh) \approx (0.8, 25.2)$ and less than 5% up to $(\Omega, kh) \approx (0.9, 32)$. The largest errors occur in the subharmonic

transfer function in the upper right corner just below the diagonal, where the ratio goes to 2.4. Above the diagonal (right upper corner) the ratio goes to 1.06, while the ratio becomes 1.1 in the upper left corner and as well as in the lower right corner.

4.2. *Finite-amplitude analysis for strongly nonlinear steady waves*

In this section, we investigate a spectral solution of the new equations for highly nonlinear steady waves, and compare it to a spectral solution of the exact equations. The analysis is restricted to one horizontal dimension and to a constant depth and it involves the governing equations (1), (2), (3) and (22*a*) combined with (15*a*, *b*), (16*a*, *b*) and (17*a*, *b*). Fenton (1988) formulated the problem in terms of the stream function, which provides some computational advantages, due to the relative simplicity of the kinematic surface condition. Here we use a slightly different procedure, which is closer to our formulation of the new Boussinesq equations.

In a frame of reference moving at the speed c, the problem is steady and the free surface conditions (1) and (2) reduce to

$$-\tilde{w} + \tilde{u}\eta_x = 0, \quad g\eta + \frac{\tilde{u}^2}{2} + \frac{\tilde{w}^2}{2} = R, \tag{33}$$

where R is the Bernoulli constant. The new Boussinesq equations can be solved to a very high degree of accuracy in the following way: First we expand the surface elevation and the velocity variables at $\hat{z}$ in terms of the Fourier series

$$\eta(x) = \sum_{j=1}^{M} A_j \cos(jkx), \tag{34a}$$

$$\hat{u}^*(x) = \bar{u} + \sum_{j=1}^{M} B_j \cos(jkx), \quad \hat{w}^*(x) = \sum_{j=1}^{M} C_j \sin(jkx). \tag{34b}$$

Next, the bottom boundary condition leads to the constraint

$$C_j = \lambda_j \left(\frac{1 + \frac{1}{9}\lambda_j^2 + \frac{1}{945}\lambda_j^4}{1 + \frac{4}{9}\lambda_j^2 + \frac{1}{63}\lambda_j^4} \right) B_j, \quad \lambda_j = jk(h + \hat{z}). \tag{34c}$$

Now (17*a*, *b*) is used to establish a connection between $\tilde{u}, \tilde{w}$ and u_0, w_0 while (15*a*, *b*) and (16*a*, *b*) are used to establish the connection between u_0, w_0 and $\hat{u}^*, \hat{w}^*$. Given the four inputs H (wave height), h (water depth), L (wavelength), and $\bar{u}_E$ (the mean Eulerian velocity), there are three kinematic constraints,

$$H = \eta(0) - \eta\left(\frac{L}{2}\right), \quad c = \frac{L}{T}, \quad c + \bar{u} - \bar{u}_E = 0,$$

plus the free-surface boundary conditions (33). The dynamic surface condition is applied at $M+1$ equally spaced points from the wave trough to wave crest, while the kinematic condition is applied at M staggered points (mid-way between the others). This gives $2M+4$ nonlinear equations for the unknowns T (wave period), $c, \bar{u}, R$ and the coefficients A_j and B_j. The system is readily solved using Newton's method with linear theory as the initial conditions. With slight modifications, the same technique

can be used to solve the fully dispersive problem simply by replacing (34b) by

$$u(x,z) = \bar{u} + \sum_{j=1}^{M} B_j \frac{\cosh(jk(z+h))}{\cosh(jkh)} \cos(jkx),$$

$$w(x,z) = \sum_{j=1}^{M} B_j \frac{\sinh(jk(z+h))}{\cosh(jkh)} \sin(jkx).$$

First, we consider the case of a highly nonlinear deep-water wave with $h/L = 0.135$ and $kh = 10$ and the results are computed with $\sigma = -0.5$. Figure 4(a) shows the spatial variation of the horizontal surface velocity normalized by the wave celerity, which is 1.09 times the linear celerity. The result is in perfect agreement with the exact solution. In figure 4(b) we show the corresponding vertical distribution of the horizontal velocity under the wave crest. Again this is in good agreement with the stream function solution (full line) over the entire water column although small discrepancies can be noticed below the still-water datum. Finally, in figure 5 we show the relative errors of the computed horizontal crest velocities for $H/L = 0.12$ and using two different values of σ. Note that with an error bound of 2% we find that $\sigma = -0.5$ is limited by $kh < 25$ while $\sigma = -0.2$ is limited by $kh < 39$. For reference figure 5 also includes a computation using (15a, b) and (16a, b) all the way to the free surface, and obviously this is much less accurate than the combination of (15a, b) and (17a, b).

5. Numerical solution procedure

In order to solve more general problems, a finite-difference solution to the new equations has been developed in a single horizontal dimension. N equally spaced points are distributed along the x-axis, and the equations are enforced at these N points. All continuous derivative operators are replaced by finite-difference approximations. This results in a set of matrix equations

$$[\tilde{u}] = \boldsymbol{A}_1[u_0] + \boldsymbol{B}_1[w_0], \quad [\tilde{w}] = -\boldsymbol{B}_1[u_0] + \boldsymbol{A}_1[w_0], \tag{35a, b}$$

$$[u_0] = \boldsymbol{A}_2[\hat{u}^*] + \boldsymbol{B}_2[\hat{w}^*], \quad [w_0] = -\boldsymbol{B}_2[\hat{u}^*] + \boldsymbol{A}_2[\hat{w}^*], \tag{35c, d}$$

and

$$\boldsymbol{A}_3[\hat{\boldsymbol{u}}^*] + \boldsymbol{B}_3[\hat{w}^*] = 0, \tag{35e}$$

where a quantity in square brackets represents a vector of values at the N grid points. The $\boldsymbol{A}_i$ and $\boldsymbol{B}_i$ (for $i = 1, 2, 3$) are the finite-difference matrices resulting from discretization of (17a, b), (15a, b) and (22b). If (3) is invoked, (35a–e) can be written as the following linear system of equations:

$$\begin{pmatrix} \boldsymbol{A}_1 - [\eta_x]\boldsymbol{B}_1 & \boldsymbol{B}_1 + [\eta_x]\boldsymbol{A}_1 & 0 & 0 \\ -\boldsymbol{I} & 0 & \boldsymbol{A}_2 & \boldsymbol{B}_2 \\ 0 & -\boldsymbol{I} & -\boldsymbol{B}_2 & \boldsymbol{A}_2 \\ 0 & 0 & \boldsymbol{A}_3 & \boldsymbol{B}_3 \end{pmatrix} \begin{pmatrix} [u_0] \\ [w_0] \\ [\hat{u}^*] \\ [\hat{w}^*] \end{pmatrix} = \begin{pmatrix} [\tilde{V}] \\ 0 \\ 0 \\ 0 \end{pmatrix}, \tag{36}$$

where $\boldsymbol{I}$ is the identity matrix. This system determines $(u_0, w_0, \hat{u}^*, \hat{w}^*)$ for given values of $(\eta, \tilde{V})$ at each grid point. Using the solution in (35b) then provides $\tilde{w}$, which allows the free-surface boundary conditions to be stepped forward in time and the process repeated.

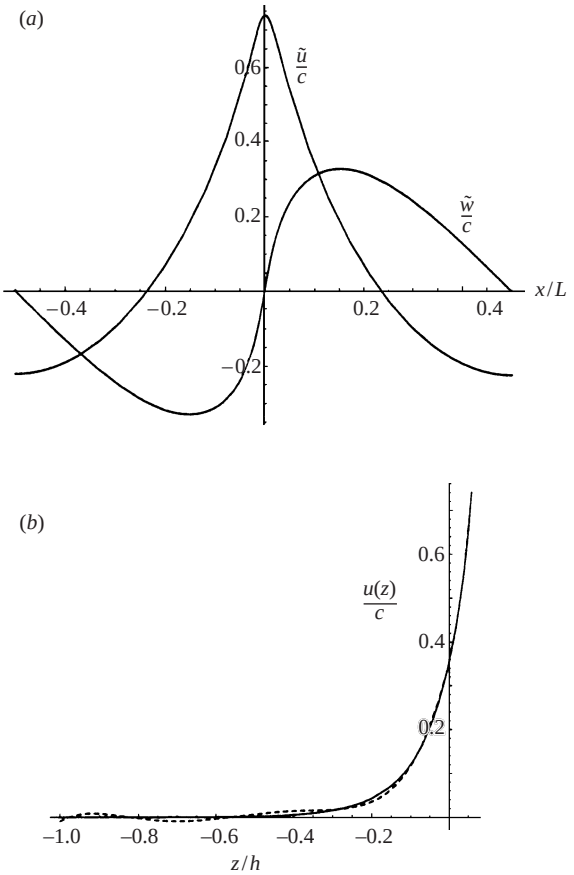

FIGURE 4. Steady deep water wave with $kh = 10$ and $H/L = 0.135$. (a) The spatial variation of the horizontal and vertical surface velocities. (b) The vertical distribution of the horizontal velocity under the wave crest. Full line: exact stream-function solution; dashed line: new formulation with $\sigma = -0.5$.

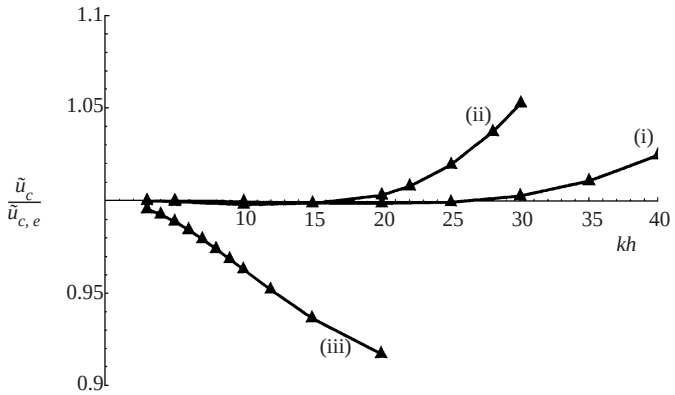

FIGURE 5. Errors in the horizontal crest velocity ($\tilde{u}_c$) relative to the stream-function solution ($\tilde{u}_{c,e}$). Steady waves with $H/L = 0.12$. (i) New formulation with a combination of (15a, b) and (17a, b) for $\sigma = -0.2$; (ii) new formulation with a combination of (15a, b) and (17a, b) for $\sigma = -0.5$; (iii) using (15a, b) from the bottom to the free surface and $\sigma = -0.5$.

In order to apply up to fifth-derivative operators, a minimum stencil size of seven points is used. All derivatives make use of the entire stencil which means that lower derivatives are of higher accuracy than higher ones. The fifth-order Cash–Karp–Runge–Kutta scheme is used for the time integration, which provides a running estimate of the error. This scheme is generally stable, although high-frequency instabilities are encountered when the waves become extremely nonlinear. Savitsky–Golay smoothing is applied at the stencil size, in order to continue these highly nonlinear calculations.

Each of the matrices $\boldsymbol{A}_i$ and $\boldsymbol{B}_i$ is banded with at least seven bands, which gives the system as written in (36) a fairly complicated sparsity structure. However, a simple re-ordering of the variables, where all velocities and equations at each grid point are grouped together, will reduce the matrix in (36) to a banded form with at least 25 bands. Since $\boldsymbol{A}_1$ and $\boldsymbol{B}_1$ are time-dependent, the matrix must be re-built and factored at each time step, but the work is still $O(N)$ since the matrix is banded.

In many cases, an explicit iteration procedure (e.g. Dommermuth & Yue 1987) can be used to satisfy the nonlinear free-surface conditions, effectively replacing (35a, b) with multiple solutions of (35c) and (35e). In this case the smaller time-independent system reads

$$\begin{pmatrix} \boldsymbol{A}_2 & \boldsymbol{B}_2 \\ \boldsymbol{A}_3 & \boldsymbol{B}_3 \end{pmatrix} \begin{pmatrix} [\hat{u}^*] \\ [\hat{w}^*] \end{pmatrix} = \begin{pmatrix} [u_0] \\ 0 \end{pmatrix}. \tag{37}$$

This can be LU-factored once and for all, and the solution obtained by J back-substitutions at each time step (where J, the number of nonlinear iteration steps, is typically 4 or 5). This leads to a substantial reduction in the total effort of solution.

6. Numerical results

In this section we consider several applications of the model, all of which are severe tests normally beyond the reach of conventional Boussinesq-type formulations: (a) computation of surface profile and interior kinematics in steady highly nonlinear solitary waves; (b) reflection of solitary waves from a vertical wall; (c) sideband instability of nonlinear deep-water wave trains; (d) nonlinear shoaling up to the point of breaking on a mildly sloping beach. While (a)–(c) are on a constant depth, (d) deals with the case on an uneven bottom bathymetry. While (a) and (b) deal with highly nonlinear waves in shallow water, (c) involves modulational instability and wave–wave interactions in deep water.

6.1. *The kinematics of high solitary waves*

The problem considered in this section is that of a solitary wave propagating on a fluid at rest over a horizontal bottom. Major contributions to the theoretical understanding of this phenomenon are due to Russell (1838), Boussinesq (1872), Rayleigh (1876), Yamada (1957), Longuet-Higgins & Fenton (1974), Miles (1980), Williams (1985) and Tanaka (1986). Among these, the most striking discovery is probably due to Longuet-Higgins & Fenton, who found that quantities such as wave celerity, mass, momentum and energy for the solitary wave all attain a maximum value for a wave of less than maximum height. Furthermore, it is generally acknowledged that the numerical results of Williams (1985) and Tanaka (1986) are extremely accurate even for the highest waves and we shall use these as reference solutions in the following verification.

We consider a constant water depth of 1.0 m, a grid size of 0.05 m and a time step of 0.025 s. The boundary conditions at the end of the model domain are determined

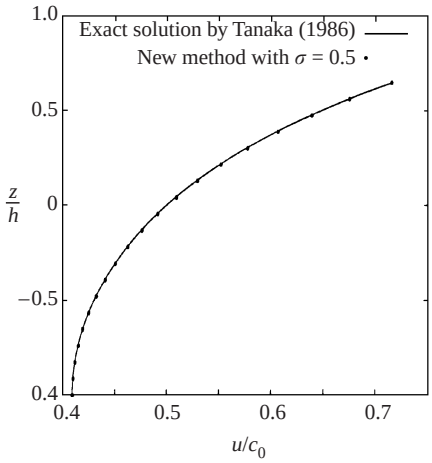

FIGURE 6. The vertical profile of the horizontal velocity under the crest of a solitary wave. $h = 1.0\,\mathrm{m}$, $a/h = 0.65$, $c/c_0 = 2.653$, $\mathrm{d}x = 0.05\,\mathrm{m}$, $\mathrm{d}t = 0.025\,\mathrm{s}$. Computed with $\sigma = -0.5$.

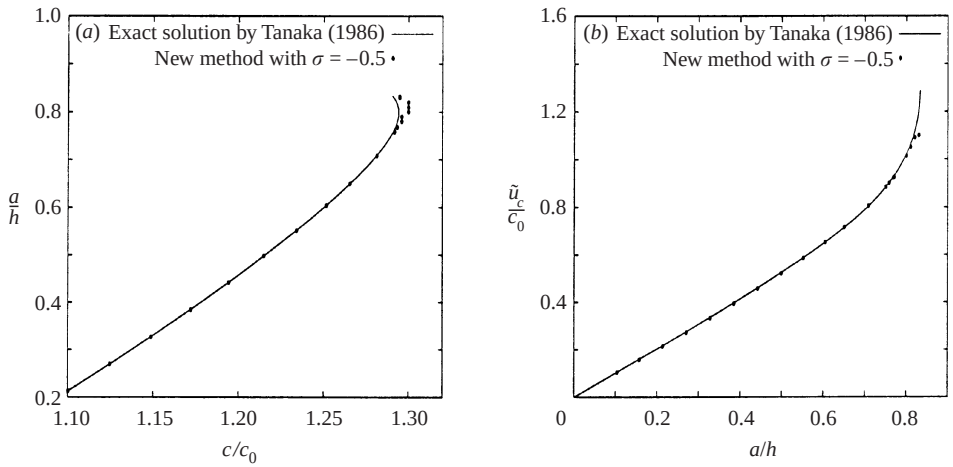

FIGURE 7. The wave celerity and the crest velocity versus wave amplitude for solitary waves. $h = 1.0\,\mathrm{m}$, $\mathrm{d}x = 0.05\,\mathrm{m}$, $\mathrm{d}t = 0.025\,\mathrm{s}$. Computed with $\sigma = -0.5$.

by computing the surface elevation and the surface velocity directly from Tanaka's solution. Any discrepances between the input solution and the approximate solitary wave solution to the Boussinesq equations will show up as a dispersive tail which is left behind. The higher the solitary wave, the faster the dispersive tail will separate from the main wave due to amplitude dispersion, and the faster a new wave of permanent form will be achieved. The celerity of the wave is determined by letting the established permanent-form solution propagate further over a distance of 10–20 times the water depth, tracking the position of the crest of the wave.

At this resolution, the initial conditions by Tanaka (1986), turn out to be steady up to a steepness of $a/h = 0.75$, after which some small tails begin to appear. However, more impressive is the comparison of the vertical distribution of the horizontal velocity, as shown in figure 6 for $a/h = 0.65$, which is seen to be in almost perfect agreement with Williams' profile all the way from the sea bed to the free surface. This result is clearly more accurate than what was achieved by Gobbi *et al.* (2000).

Figure 7(a, b) shows the wave celerity and crest velocity for a number of solitary waves, varying the relative amplitudes a/h from 0.1 to 0.83. Again an excellent agreement with Williams' solution is obtained except for the highest waves. Inaccuracies do occur for relative amplitudes a/h higher than 0.78 and the problem is most likely connected to the sharpening of the wave crest, which for the highest solitary waves rapidly approaches the limiting angle of 120°. This makes it difficult to resolve the finest details with a finite-difference formulation and it is expected that numerical diffusion is introduced by the successive use of fifth-order spatial derivatives, a problem which was also recognized by Gobbi *et al.* (2000).

6.2. *Reflection of solitary waves from a vertical wall*

In this section we study nonlinear reflection of high-amplitude solitary waves from a vertical wall. When low-amplitude solitary waves collide with a vertical wall they may behave as solitons and reflect without reduction in height and speed. This is, however, not the case for highly nonlinear solitary waves, where the reflected wave will lose energy to a dispersive tail, so that the height and the speed of the reflected wave is smaller than before the collision. These phenomena have been studied experimentally by Maxworthy (1976), analytically by e.g. Su & Mirie (1980) and Wu (1995, 1998, 1999), and numerically by Mirie & Su (1982) who used Boussinesq equations, by Fenton & Rienecker (1982) using a Fourier method, and by Grilli & Svendsen (1990) and Cooker, Weidman & Bale (1997) using a boundary-integral method for solving the Euler equations with fully nonlinear boundary conditions.

As discussed by Cooker *et al.* (1997, hereinafter referred to as CWB97), the following sequence of events occurs during the impact of the solitary wave: Initially the incident wave propagates with constant speed and constant wave height. When the crest is less than about twice the water depth from the wall the crest accelerates significantly. At the instant t_a (the so-called attachment time) the wave crest has 'snapped through' to the wall with a corresponding elevation η_a. With some delay, at time t_0 the maximum run-up occurs with an elevation η_0, which can be several times larger than the incoming amplitude. After a further delay, the wave crest leaves the wall at t_d, the so-called detachment time, with an elevation η_d, which is always less than η_a. CWB97 found that $t_0 - t_a < t_d - t_0$, i.e. it always takes more time for the waterline to fall than to rise. The total time during which the crest is attached to the wall is called the wall residence time $t_r = t_d - t_a$. At the stage of detachment, the crest leaves the wall at a very high speed, but quickly decelerates to a constant speed which is slightly lower than the incoming speed. For small-amplitude and moderate-amplitude solitary waves there will be very little difference in wave height and wave speed compared to the perfect reflection soliton behaviour.

In the following we compare our numerical results with the boundary integral method of CWB97. Figure 8 shows a number of snapshots of the computed surface elevation for a solitary wave with $a/h = 0.7$ moving from right to left. We note that the maximum runup is somewhat smaller than the one computed by CWB97 but in both cases it is significantly larger than twice the incoming amplitude. For this highly nonlinear case our computations break down during the downrush phase, similar to the behaviour reported by CWB97. For $a/h < 0.7$, computations are stable after the reflection also, and the computed wave crest amplitudes for $a/h = 0.5$ are shown as a function of time in figure 9. The attachment and detachment times are indicated with markers and show that the elevation at the detachment time is always smaller than that at attachment. A series of simulations have been made with the nonlinearity parameter a/h ranging from 0.05 to 0.70 and we show the resulting

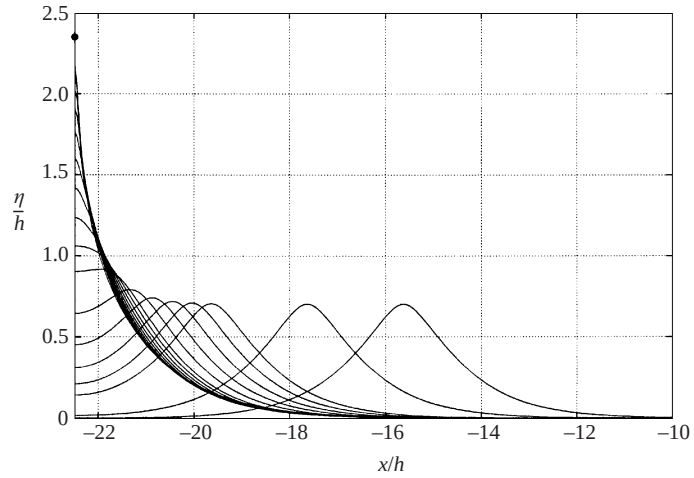

FIGURE 8. Reflection of a solitary wave from a vertical wall. Snapshots of the surface elevation moving from right to left. $a/h = 0.70$, $h = 1.0\,\mathrm{m}$, $\mathrm{d}x = 0.05\,\mathrm{m}$, $\mathrm{d}t = 0.025\,\mathrm{s}$. Computed with $\sigma = -0.5$. Dot: maximum runup as computed by CWB97.

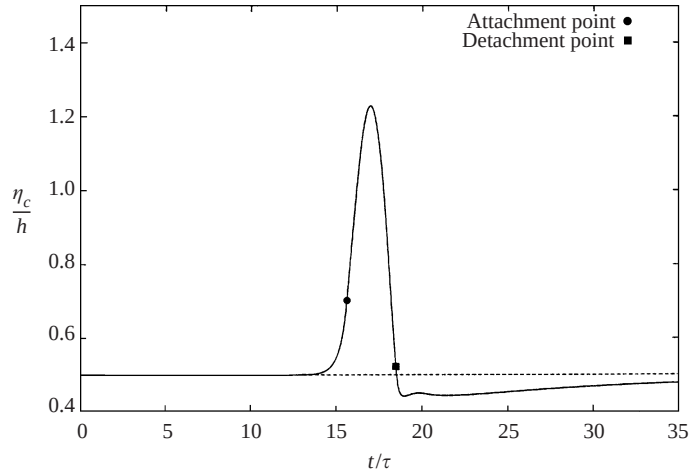

FIGURE 9. Reflection of a solitary wave from a vertical wall. Maximum surface elevation in the domain showing the attachment and detachment times. $a/h = 0.50$, $h = 1.0\,\mathrm{m}$, $\mathrm{d}x = 0.05\,\mathrm{m}$, $\mathrm{d}t = 0.025\,\mathrm{s}$. Computed with $\sigma = -0.5$.

computed attachment and detachment crest amplitudes and the maximum runup in figure 10. They are seen to be in very good agreement with the results obtained by CWB97 using their boundary-integral method.

Next, we have determined the instantaneous wall force by integrating the pressure distribution over the wall from the sea bed to the free surface. The pressure distribution is obtained by integrating the vertical Euler equation from the free surface to an arbitrary z-datum. Figure 11 shows the computed force as a function of time relative to t_0, for selected incoming values of a/h. Except for the highest waves, our computations agree very well with the results of CWB97. For $a/h = 0.6$ some discrepancies occur, especially during the downrush, but it is unlikely that any of these calculations are especially accurate due to the violence of the flow and the subsequent breakdown of the numerics.

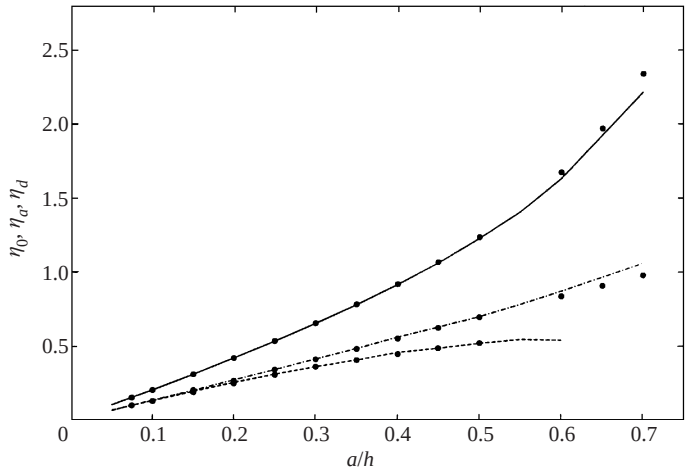

FIGURE 10. Reflection of a solitary wave from a vertical wall. Attachment amplitude, detachment amplitude and maximum runup versus incoming wave amplitude. Computed with $\sigma = -0.5$. Dashed-dot line: attachment amplitude; dashed line: detachment amplitude; full line: maximum runup. Symbols: computed by CWB97.

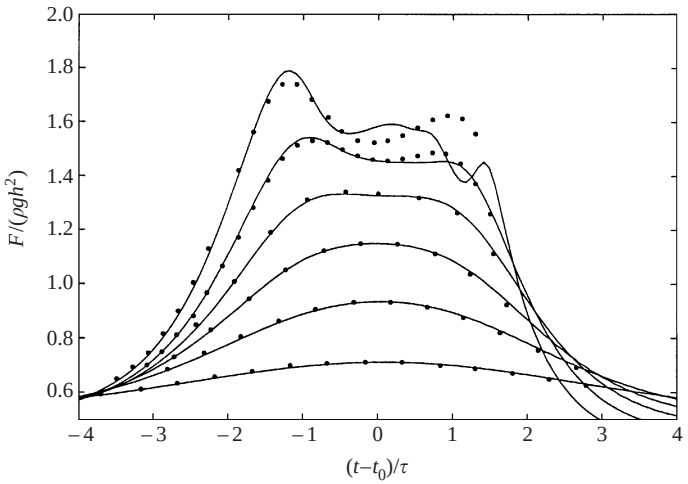

FIGURE 11. Reflection of a solitary wave from a vertical wall. Time variation of depth-integrated wall force computed for a range of different incoming wave amplitudes ($a/h = 0.1, 0.2, 0.3, 0.4, 0.5, 0.6$). Full line: computed with $\sigma = -0.5$; symbols: computed by CWB97.

The overall trend in figure 11 is that for a/h up to 0.3 the wall force is single peaked while it becomes double peaked for higher waves. The mechanism behind this variation is illustrated in figure 12, where we split up the pressure into a hydrostatic part (measured from the instantaneous position of the surface) and an acceleration part (including nonlinear velocity terms and the temporal derivative of the vertical velocity). For small waves, the force is dominated by hydrostatic pressure and it has a single maximum which occurs at t_0, i.e. at the time of maximum runup. For larger values of a/h, the vertical acceleration of the flow becomes more important, especially during the phase where the water is pushed up the wall. This increases the pressure above the hydrostatic value and a local maximum occurs before the maximum runup. During the phase of maximum runup, the acceleration forces are counteracting the

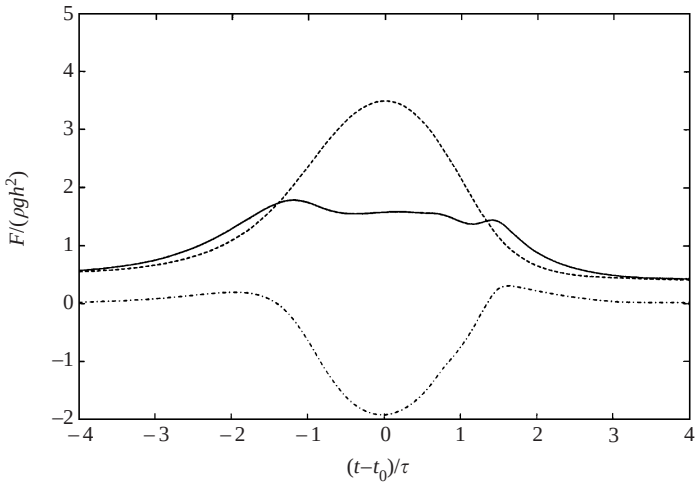

FIGURE 12. Reflection of a solitary wave ($a/h = 0.6$) from a vertical wall. Full line: total depth-integrated wall force; dashed line: static contribution; dashed-dot line: dynamic contribution.

hydrostatic forces, which leads to a local minimum. After the maximum runup, the water slides back down the wall and at the end of this descent the deceleration again increases the pressure above the hydrostatic value and creates a second slightly smaller peak in the force. We note that this double-peak pressure behaviour for highly nonlinear waves was also observed by Bredmose *et al.* (2002) in connection with wave sloshing in a tank.

6.3. *Sideband instability of nonlinear wave trains*

In this section we study modulational instability of deep water waves. Benjamin & Feir (1967) showed theoretically and experimentally that weakly nonlinear deep-water waves can be unstable to modulational perturbations under certain conditions. They considered a wave train consisting of a carrier wave at frequency ω and two small-amplitude sideband waves at frequencies $\omega(1-\delta)$ and $\omega(1+\delta)$, i.e.

$$\eta = a\cos(\omega t - kx) + \beta a\cos\Theta_1 + \beta a\cos\Theta_2,$$
$$\Theta_1 = \omega(1+\delta)t - k_1 x + \Psi_1, \quad \Theta_2 = \omega(1-\delta)t - k_2 x + \Psi_2.$$

Quartet interactions between these wave components can lead to near resonance given the conditions

$$2\omega - \omega_1 - \omega_2 = 0, \quad 2k - k_1 - k_2 = \Delta k,$$

where Δk is a wavenumber mismatch which will de-tune the resonance. For linear deep-water waves, we have

$$k = \frac{\omega^2}{g}, \quad k_1 = k(1+\delta)^2, \quad k_2 = k(1-\delta)^2, \quad \Delta k = 2k\delta^2,$$

and consequently the de-tuning will be small if δ is small. However, Benjamin & Feir showed that amplitude dispersion can eliminate the de-tuning under certain circumstances, and this will produce resonance where the sideband waves can grow exponentially. According to their theory the most unstable situation occurs when

$$\delta = ka, \quad \Psi_1 = \Psi_2 = \frac{\pi}{4}.$$

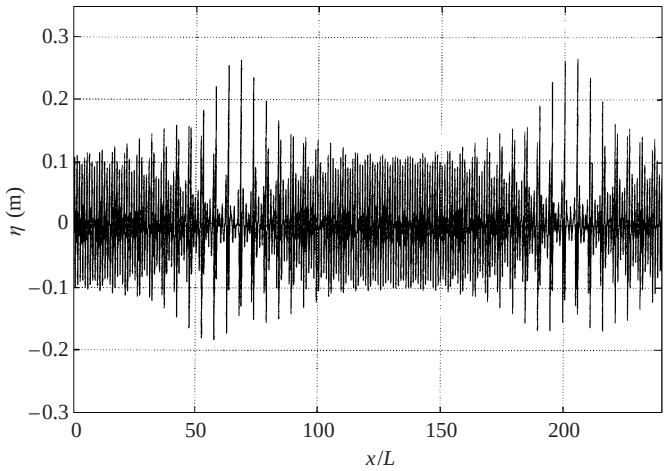

FIGURE 13. Snapshot of the spatial variation of the surface elevation for nonlinear wave trains with sideband perturbations. $h = 2\pi$ m, $T = 2.006$ s, $k = 1\,\mathrm{m}^{-1}$, $kh = 2\pi$, $ka = 0.1$, $\delta = ka$, $\beta = 0.05$, $\mathrm{d}x = 0.2$ m, $\mathrm{d}t = 0.0625$ s. Computed with $\sigma = -0.5$.

Benjamin & Feir's theory describes the onset of the instability and the initial growth of the sidebands. Higher-order stability theories have been given by e.g. Crawford *et al.* (1981) and McLean (1982), and other milestones within this field have been provided by Lake *et al.* (1977), Melville (1982) and Lo & Mei (1985).

Numerical simulations of the phenomenon of modulational instability have typically been conducted on the basis of various forms of the nonlinear Schrödinger equations, the Zakharov equations or fully nonlinear boundary integral methods. So far most simulations have been made utilizing spatially periodic boundary conditions to keep the computational domain small (see e.g. Dold & Peregrine 1986; Dommermuth & Yue 1987; Landrini *et al.* 1998; Henderson, Peregrine & Dold 1999). Exceptions are Tulin, Yao & Wang (1994) and Mayer, Garapon & Sørensen (1998), who simulated the spatial and temporal evolution in a long wave tank.

Until now, Boussinesq formulations have not been applied for this purpose, because of their shallow-water limitations. As discussed by AMS99, the accurate modelling of sideband instabilities requires an accurate description of amplitude dispersion, and of the first and second derivatives of ω with respect to k (i.e. ω_k and ω_{kk}). Of these quantities, the latter is the most critical for Boussinesq-type formulations, and AMS99 found that with a Padé [4, 4] dispersion relation the applicability would be restricted to kh up to about 3. In our present formulation, the linear dispersion relation is given by (25c) and (26) and the resulting accuracy of $\omega\omega_{kk}$ relative to the target value from fully dispersive theory can easily be determined: with a 5% error criterion we find the following limitations: $kh < 13.8$ with $\sigma = -0.5$ and $kh < 21.5$ with $\sigma = -0.2$.

6.3.1. *Recurrence*

Our first test case is inspired by Mayer *et al.* (1998), who used a fractional step method with a surface adaptive grid to solve the two-dimensional Euler equations in a tank covering about 130 wavelengths. The depth is 2π m and at the boundary a carrier wave and two sideband waves are generated. The period of the carrier wave is 2.006 s, which corresponds to $k = 1.0\,\mathrm{m}^{-1}$, i.e. a wavelength of 2π m. The initial amplitude of the carrier wave is $a = 0.1$ m, i.e. $ka = 0.1$. For the sideband waves, we use $\delta = ka$, $\beta = 0.05$ and a phase shift of $\pi/4$. We extend the computational domain

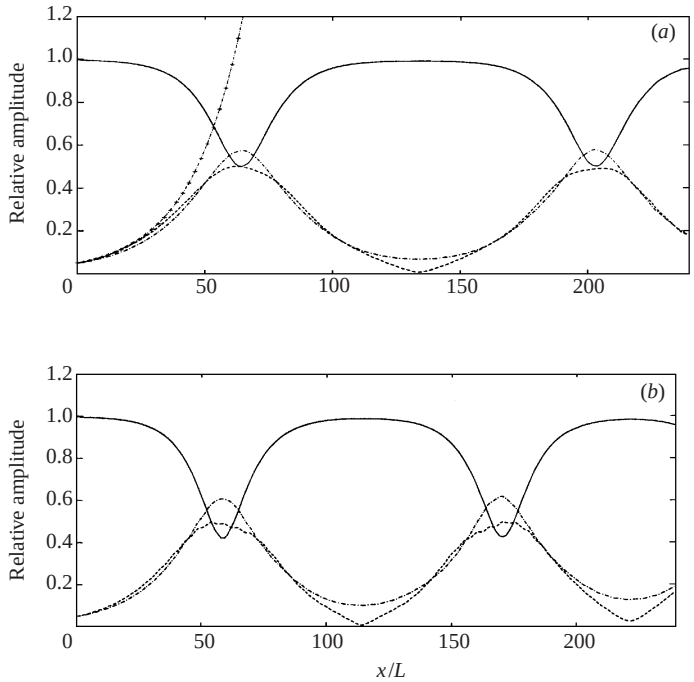

FIGURE 14. Spatial evolution of the amplitudes of the carrier wave and the two sidebands. Computed with $\sigma = -0.5$. Full line: carrier wave amplitude; dashed-dot line: lower sideband amplitude; dashed line: upper sideband amplitude; line with symbols: theoretical prediction from Benjamin & Feir theory. (*a*) Data as shown in figure 13. (*b*) As (*a*) but with $ka = 0.105$ and $\delta = 0.100$.

to cover 1600 m, i.e. approximately 250 wavelengths. An absorbing sponge layer is applied at both ends of the model domain to keep reflections to a minimum.

Figure 13 shows the computed spatial variation of the surface elevation after 1300 s. Close to the boundary we notice the weak beating between the carrier and its sidebands with a beat length of approximately 5 wavelengths. Due to the growth of the sidebands this beating increases and after 63 wavelengths we observe the formation of a massive wave pulse with amplitudes reaching 0.26 m. The process is recurrent and after 134 wavelengths the wave train has returned to its initial state. Then a new massive wave pulse appears at 204 wavelengths. We note that Mayer *et al.* (1998) found the maximum peak to be only 0.19 m, but they also found that the waves approaching the first point of recurrence at $x/L \approx 130$ had lost about 20% of their initial heights due to numerical damping. In the present simulation there is no sign of energy loss, and although the two pulses are not identical, they do reach approximately the same height.

In figure 14(*a*) we show the spatial evolution of the carrier and sideband amplitudes, and notice that the initial growth rate of the sidebands is in good agreement with Benjamin & Feir's prediction. A feature not predicted by Benjamin & Feir is that the upper sideband initially grows slightly faster than the lower one, while the lower sideband becomes larger than the upper sideband near the peak modulation. This unequal growth of lower and upper sidebands was first demonstrated in detail by Lo & Mei (1985), by using Dysthe's (1979) extension of the Schrödinger equation. The distance between the two massive wave pulses in figure 13 and between the two minima of the carrier amplitude in figure 14(*a*) is found to be 141 wavelengths. In order to validate this result, we compare with a similar investigation made by

Landrini *et al.* (1998), who used a boundary-integral method with spatially periodic boundary conditions. We transform their results from the time domain to the spatial domain using the transformation

$$\frac{x}{L} = \frac{c_g t}{cT} \approx \frac{1}{2}\,\frac{t}{T},$$

which has also previously been employed by Benjamin & Feir (1967) and Lake *et al.* (1977). With this transformation the beat length computed by Landrini (for the case of $ka = 0.100$ and $\delta = 0.10$) is approximately 140 wavelengths, i.e. in excellent agreement with our result.

Landrini *et al.* also investigated the accuracy of the cubic Schrödinger equation (NLS) and a Hamiltonian method by Krasitskii (1994). For the case of $ka = 0.100$ and $\delta = 0.10$, they found that Krasitskii's method was very accurate, while the NLS resulted in a beat length of only 108 wavelengths, i.e. 23% in error. Stiassnie & Kroszynski (1982) derived the following analytical solution based on the NLS equations:

$$\frac{L_{beat}}{L} = \frac{c_g}{c}\frac{T_{beat}}{T} \approx \frac{c_g}{c}\left(\frac{1.674 - 4\ln\beta}{2\pi(ka)^2}\right),$$

and this leads to a beat length of 108.7 m, i.e. in good agreement with Landrini *et al.*'s numerical solution of the NLS.

In a further investigation, Landrini *et al.* concluded that with a small increase in ka, the relative performance of Krasitskii's method rapidly deteriorated in the second cycle of modulation and for the case of $ka = 0.105$ and $\delta = 0.10$, they found the correct beat length to be 113 wavelengths, while Krasitskii's method resulted in 135 wavelengths. Our computation of this test case is shown in figure 14(b) and with a beat length of 112 wavelengths it is in very good agreement with Landrini's result.

6.3.2. *Frequency downshift*

Wind-wave spectra are known to shift towards lower frequencies as the fetch increases. In an energy-conserving two-dimensional system, a local frequency downshift will occur near the peak of modulation due to the unequal growth of the sidebands, but no permanent downshift will occur because the modulational process will be cyclic as demonstrated in the previous example. In contrast, the experiments by Melville (1982) showed that for steeper waves breaking typically occurs at the peak of the modulation, i.e. when the lower sideband is at its maximum, and this opens up for a permanent downshift of the peak frequency.

The phenomenon of frequency downshift has been modelled with Dysthe's fourth-order Schrödinger equations by Lo & Mei (1985), who examined the effect of viscous dissipation due to friction; by Trulsen & Dysthe (1990), who incorporated the effect of wave breaking by introducing a damping term activated for waves exceeding a certain height; and by Hara & Mei (1991), who modelled the forcing by a weak wind and the damping by eddy viscosity. These efforts, amongst others, indicate that downshift of two-dimensional Stokes waves appears to be related to damping effects in a rather insensitive manner, and, without any dissipative effects added, permanent shift of the peak frequency does not occur in two dimensions. In three dimensions, it turns out that a permanent downshift can occur without the influence of dissipation, as demonstrated by Trulsen & Dysthe (1997), who investigated the effect of oblique sideband modulation.

Recently, Tulin & Waseda (1999) conducted a number of seeded experiments to investigate the importance of wave breaking for modulational instability. In the

absence of wave breaking, they observed near recurrence as discussed above, although complete recurrence was prevented by some energy transfer to higher frequencies. In experiments involving local wave breaking, they found (in their figure 18) an overall decrease of the carrier wave as well as of the higher sideband, while the lower sideband was increased relative to the non-breaking event. As a result a state of downshifting took place with the carrier wave and the lower sideband nearly coinciding in magnitude.

In the following, we consider one of their test cases involving a brief event of wave breaking near the first modulational peak. We use a depth of 1.2 m (rather than the 2.1 m used in the experiment), a carrier wave of frequency 1.14 Hz (wavelength 1.2 m) and a wave steepness $ka = 0.133$. The sideband waves are generated at the boundary at frequencies 1.029 Hz and 1.267 Hz (corresponding to $\delta = 0.785ka$) with relative amplitudes $\beta = 0.03$. Two simulations have been made with grid sizes of 0.05 m and 0.025 m, respectively, and the results are almost identical except in the vicinity of the first modulation peak. In this region the waves become very steep, and while the coarse-grid simulation survives, the fine-grid simulation eventually breaks down, indicating the necessity of a breaking model. The coarse-grid results are shown in figure 15(*a*). At the first modulational peak, which occurs at $x/L \approx 44$, the carrier mode has a local minimum, while the lower and upper sidebands increase to a local maximum. At this point the lower sideband is by far the largest of the three. Beyond this point, the trend in figure 15(*a*) deviates from figure 14(*a*, *b*) as the lower sideband starts to oscillate around a much higher mean level and never returns to its initial very low level, while the upper sideband stays at a considerably lower mean level than the lower sideband. This increase of asymmetry between the lower and upper sidebands indicates an effective frequency downshift, and as a result the wave train starts to vary between two extreme states: a state with dominant lower sideband and insignificant carrier wave and a state where the lower sideband and the carrier are of almost equal size.

Tulin & Waseda concluded that frequency downshift cannot occur unless dissipation is involved. Our model results do not contradict this conclusion, because although we have not attempted to model the local wave breaking occurring at the first peak of modulation, the relatively coarse grid resolution has apparently introduced a certain amount of numerical dissipation. As a result, our coarse-grid results turn out to agree fairly well with the experimental results of Tulin & Waseda, as shown in a close-up in figure 15(*b*). Notice that beyond the first modulational point at $x/L \approx 44$, we slightly underestimate the lower sideband and slightly overestimate the carrier wave. This indicates that our model results involve some, but too little, dissipation compared to the experimental results. Obviously the way to proceed is to refine the grid size and to introduce a breaking module in the model. This work is in progress.

6.4. *Nonlinear shoaling on a mildly sloping beach*

Ting & Kirby (1994) presented measurements for spilling breakers on a plane sloping beach with a slope of 1/35 starting at a depth of 0.40 m. As input they generated regular waves with a wave period of 2.0 s and a wave height of 0.125 m. At the boundary, we generate a stream-function solution with these parameters. Our model does not yet include the feature of wave breaking, and instead we absorb the shoaling waves with a sponge layer placed in the region from $x = 6$ m to $x = 10$ m (see figure 16). This figure shows snapshots of the computed spatial variation of the surface elevation, and the envelope is seen to be extremely regular without undulations.

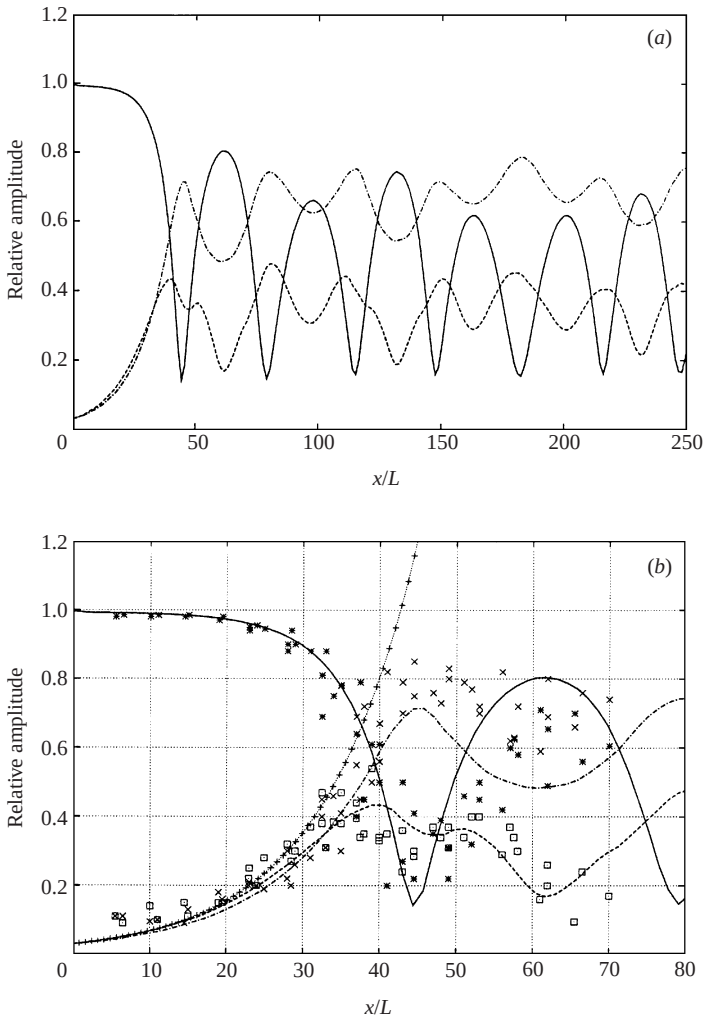

FIGURE 15. (*a*) Spatial evolution of the amplitudes of the carrier wave and the two sidebands. $h = 1.2\,\mathrm{m}$, $f = 1.14\,\mathrm{Hz}$, $1.029\,\mathrm{Hz}$ and $1.267\,\mathrm{Hz}$, $kh = 6.28$, $ka = 0.133$, $\delta = 0.785ka$, $\beta = 0.03$, $\mathrm{d}x = 0.05\,\mathrm{m}$, $\mathrm{d}t = 0.05\,\mathrm{s}$. Full line: carrier wave amplitude; dashed-dot line: lower sideband amplitude; dashed line: upper sideband amplitude. Computed with $\sigma = -0.5$. (*b*) Same as (*a*) but including measurements by Tulin & Waseda (1999), for lower sideband (cross), upper sideband (square), carrier wave (star). Dotted line with plus symbols: theoretical prediction from Benjamin & Feir theory.

This confirms that the model equations support the stream-function solution without releasing spurious higher harmonics. Up to the point of initial breaking at $x = 6\,\mathrm{m}$, the experimental data of the crest and trough elevations is in excellent agreement with the computations, and the only difference is a small amount of reflection which shows up in the measured data due to the process of wave breaking. Our sponge layer does not reflect any noticeable amount of energy, but naturally the rate of decay inside the sponge region is quite different from the measured decay.

Figure 17 shows a comparison of the computed and measured wave profile at the point of initial breaking ($x = 6.0\,\mathrm{m}$) and we notice a remarkable agreement between the profiles. Only in the trough region do some minor discrepances show up as the

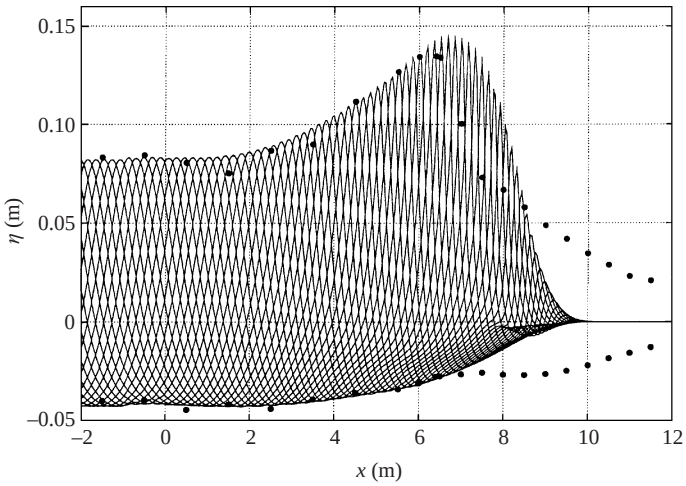

FIGURE 16. Nonlinear shoaling. Snapshots of the computed spatial variation of the surface elevation. Symbols: experimental data from Ting & Kirby (1994) showing wave crest elevation and wave trough elevation. Sloping beach with slope 1/35 starting in a depth of 0.4 m. Calculated using: stream-function theory, wave period 2.0 s and height 0.125 m, with $\sigma = -0.5$.

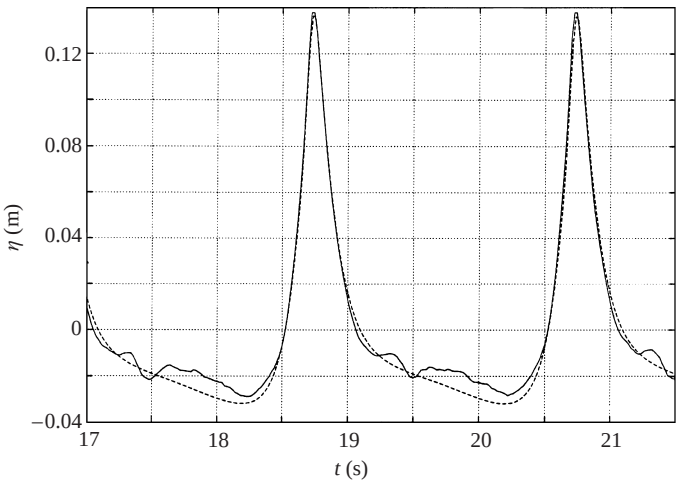

FIGURE 17. Nonlinear shoaling. Time series of the surface elevation near the point of incipient breaking. Full line: computed with $\sigma = -0.5$. Dotted line: experimental data from Ting & Kirby (1994). Data as shown in figure 16.

experimental data contain higher harmonics which are absent in the computation. We can conclude that, in a future breaking model, it will be possible to use physically realistic measures for breaking criteria. Such a model is at present being developed and will be reported later.

7. Summary and conclusions

A new Boussinesq-type method has been presented with the objective of improving the accuracy of the vertical variation of the velocity field as well as the accuracy of linear and nonlinear properties. The method is applicable to highly nonlinear waves in shallow water as well as to highly nonlinear and dispersive waves in deep water. It

is restricted to mildly sloping bathymetries but can be extended to steeper slopes. The derivation procedure involves a number of steps, which turn out to be key elements in achieving highly accurate solutions.

First, the dynamic and kinematic conditions at the free surface are expressed in terms of velocity variables defined directly on the free surface and, as pointed out by AMS99, the time-stepping of these exact equations ensures that nonlinear and linear properties are equally accurate, in contrast to conventional Boussinesq formulations.

Second, the velocity field is found as an approximate solution to the Laplace equation and it is expressed in terms of finite series expansions involving the horizontal and vertical velocity components at an arbitrary z-level, $\hat{z}$. This z-level, which is assumed to be a constant fraction of the still-water depth, is determined by minimizing the depth-integrated error of the linear velocity profile (leading to the choice of $\hat{z} = -0.5h$). However, the possibility of minimizing the error in linear dispersion is also investigated (leading to the choice of $\hat{z} = -0.2h$).

Third, we keep the vertical velocity component at $\hat{z}$ as an unknown and avoid to expressing it in terms of the horizontal component via the truncated tan-operator at the sea bottom. This is the key to avoid introducing severe restrictions on the radius of convergence of the velocity expansions, which occurs in most other Boussinesq formulations (see Madsen & Agnon 2002).

Fourth, the introduction of pseudo-velocity variables and a further operator manipulation of the kinematic condition at the sea bottom brings Padé approximants into the linear dispersion relation, as well as further improving the accuracy of the velocity profile.

As a result, the linear dispersion relation becomes a Padé [8, 10] type expansion of the fully dispersive solution and this expression turns out to be highly accurate for kh as high as 25 for $\hat{z} = -0.5h$ and 40 for $\hat{z} = -0.2h$. Generally speaking, the nonlinear properties are as accurate as the linear properties and as shown in § 4, an error bound of 2% in the crest velocity allows us to use the method up to $kh \approx 25$ for $\hat{z} = -0.5h$ and to 39 for $\hat{z} = -0.2h$. If the vertical variation of the velocity profile and of the pressure is of interest, $\hat{z} = -0.5h$ should be chosen and in this case high accuracy can be obtained even for highly nonlinear waves up to $kh \approx 12$. In fact it is also possible to use $\hat{z} = -0.2h$, but in this case the analytical velocity coefficients (16a, b) should be replaced by numerically optimized coefficients as discussed by Madsen *et al.* (2002).

Finally, we emphasize that the concept presented in this paper is by no means limited to a formulation including fifth-derivative operators. For some purposes it may be more attractive to use a formulation limited to third-derivatives, in which case the computational effort as well as the accuracy will be less. Such possibilities, together with two other ways of truncating the infinite series expansions, are presented and analysed in Madsen *et al.* (2002). It should also be mentioned that a completely different Boussinesq-type approach has been pursued by Bingham, Agnon & Madsen (2002), which presents a Fourier–Boussinesq formulation which involves the inclusion of a Fourier transform.

This work was financially supported by the Danish Technical Research Council (STVF grant no. 9801635). Inspiring discussions with Dr Hemming Schäffer are also acknowledged.

REFERENCES

Agnon, Y., Madsen, P. A. & Schäffer, H. A. 1999 A new approach to high order Boussinesq models. *J. Fluid Mech.* **399**, 319–333 (referred to herein as AMS99).

Benjamin, T. B. & Feir, J. E. 1967 The disintegration of wave trains on deep water. Part 1. Theory. *J. Fluid Mech.* **27**, 417–430.

Bingham, H. B., Agnon, Y. & Madsen, P. A. 2002 A fully dispersive Fourier-Boussinesq method for nonlinear surface waves. Submitted for publication to *Proc. R. Soc. Lond.*

Boussinesq, J. 1872 Théorie des ondes et des remous qui se propagent le long d'un canal rectangulaire horizontal, en communiquant au liquide contenu dans ce canal des vitesses sensiblement pareilles de la surface au fond. *J. Math. Pures Appl.* **17**, 55–108.

Bredmose, H., Brocchini, M., Peregrine, D. H. & Thais, L. 2002 Experimental investigation and numerical modelling of steep forced water waves. Submitted for publication to *J. Fluid Mech.*

Chen, Y. & Liu, P. L.-F. 1995 Modified Boussinesq equations and associated parabolic models for water wave propagation. *J. Fluid Mech.* **288**, 351–381.

Cooker, M. J., Weidman, P. D. & Bale, D. S. 1997 Reflection of a high-amplitude solitary wave at a vertical wall. *J. Fluid Mech.* **342**, 141–158 (referred to herein as CWB97).

Crawford, D. R., Lake, B. M., Saffman, P. G. & Yuen, H. C. 1981 Stability of weakly nonlinear deep-water waves in two and three dimensions. *J. Fluid Mech.* **105**, 177–191.

Dean, R. G. & Sharma, J. N. 1981 Simulation of wave systems due to nonlinear directional spectra. *Proc. Intl Symp. Hydrodynamics in Ocean Engng*, vol. 2, pp. 1211–1222. The Norwegian Inst. of Technol.

Dold, J. W. & Peregrine, D. H. 1986 Water-wave modulation. *Proc. 20th Intl Conf. on Coastal Engng, Taipei*, vol. 1, pp. 163–175. ASCE.

Dommermuth, D. G. & Yue, D. K. P. 1987 A high-order spectral method for the study of nonlinear gravity waves. *J. Fluid Mech.* **184**, 267–288.

Dysthe, K. B. 1979 Note on a modification to the nonlinear Schrödinger equation for application to deep water waves. *Proc. R. Soc. Lond.* A **369**, 105–114.

Fenton, J. D. 1988 The numerical solution of steady water wave problems. *Comput. Geosci.* **14**, 357–368.

Fenton, J. D. & Rienecker, M. M. 1982 A Fourier method for solving nonlinear water-wave problems: application to solitary-wave interactions. *J. Fluid Mech.* **118**, 411–443.

Gobbi, M. F., Kirby, J. T. & Wei, G. 2000 A fully nonlinear Boussinesq model for surface waves. Part 2. Extension to $O(kh)^4$. *J. Fluid Mech.* **405**, 181–210.

Grilli, S. & Svendsen, I. A. 1990 The propagation and runup of solitary waves on steep slopes. *CACR Rep.* 91-04. University of Delaware, USA.

Hara, T. & Mei, C. C. 1991 Frequency downshift in narrowbanded surface waves under the influence of wind. *J. Fluid Mech.* **230**, 429–477.

Henderson, K. L., Peregrine, D. H. & Dold, J. W. 1999 Unsteady water wave modulations: fully nonlinear solutions and comparison with the nonlinear Schrödinger equation. *Wave Motion* **29**, 341–361.

Krasitskii, V. P. 1994 On reduced equations in the Hamiltonian theory of weakly nonlinear surface waves. *J. Fluid Mech.* **272**, 1–20.

Lake, B. M., Yuen, H. C., Rungaldier, H. & Ferguson, W. E. 1977 Nonlinear deep-water waves: theory and experiment. Part 2. Evolution of a continuous wave train. *J. Fluid Mech.* **83**, 49–74.

Landrini, M., Oshri, O., Waseda, T. & Tulin, M. P. 1998 Long time evolution of gravity wave systems. In *Proc. 13th Intl Workshop on Water Waves and Floating Bodies* (ed. A. J. Hermans), *Alphen aan den Rijn*, pp. 75–78.

Lo, E. & Mei, C. C. 1985 A numerical study of water-wave modulation based on a higher-order nonlinear Schrödinger equation. *J. Fluid Mech.* **150**, 395–416.

Longuet-Higgins, M. S. & Fenton, J. D. 1974 On the mass, momentum, energy and circulation of a solitary wave. II. *Proc. R. Soc. Lond.* A **340**, 471–493.

Madsen, P. A. & Agnon, Y. 2002 On the accuracy and convergence of velocity kinematics in the framework of Boussinesq theory. Submitted for publication.

Madsen, P. A., Bingham, H. B. & Schäffer, H. A. 2002 Boussinesq-type formulations for fully nonlinear and extremely dispersive water waves: Derivation and Analysis. To appear in *Proc. R. Soc. Lond.*

Madsen, P. A. & Schäffer, H. A. 1998 Higher order Boussinesq-type equations for surface gravity waves – Derivation and analysis. *Phil. Trans. R. Soc. Lond.* A **356**, 1–59.

Madsen, P. A. & Schäffer, H. A. 1999 A review of Boussinesq-type equations for gravity waves. In *Advances in Coastal and Ocean Engineering*, vol. 5 (ed. P. Liu), pp. 1–95. World Scientific.

Madsen, P. A. & Sørensen, O. R. 1993 Bound waves and triad interactions in shallow water. *Ocean Engng* **20**, 359–388.

Maxworthy, T. 1976 Experiments on collisions between solitary waves. *J. Fluid Mech.* **116**, 207–225.

Mayer, S. T., Garapon, A. & Sørensen, L. S. 1998 A fractional step method for unsteady free-surface flow with applications to nonlinear wave dynamics. *Intl J. Numer. Meth. Fluids* **28**, 293–315.

McLean, J. W. 1982 Instabilities of finite amplitude water waves. *J. Fluid Mech.* **114**, 315–330.

Melville, W. K. 1982 The instability and breaking of deep-water waves. *J. Fluid Mech.* **115**, 165–185.

Miles, J. W. 1980 Solitary waves. *Annu. Rev. Fluid Mech.* **12**, 11–43.

Mirie, R. M. & Sue, C. H. 1982 Collisions between two solitary waves. *J. Fluid Mech.* **115**, 475–492.

Nwogu, O. 1993 Alternative form of Boussinesq equations for nearshore wave propagation. *J. Waterways, Port, Coastal, Ocean Engng, ASCE* **119**, 618–638.

Ottesen-Hansen, N.-E. 1978 Long period waves in natural wave trains. *Prog. Rep.* 46, pp. 13–24. Inst. of Hydrodyn. and Hydraulic Engng. (ISVA), Tech. University of Denmark.

Peregrine, D. H. 1967 Long waves on a beach. *J. Fluid Mech.* **27**, 815–827.

Rayleigh, Lord 1876 On waves. *Phil. Mag.* (5) **1**, 257–279.

Russell, J. S. 1838 Report of the Commitee on waves. *Rep. Meet. Br. Assoc. Adv. Sci. 7th. Liverpool*, pp. 417–496. John Murray, London.

Sand, S. E. & Mansard, E. P. D. 1986 Reproduction of higher harmonics in irregular waves. *Ocean Engng* **13**, 57–83.

Schäffer, H. A. 1996 Second-order wavemaker theory for irregular waves. *Ocean Engng* **23**, 47–88.

Schäffer, H. A. & Madsen, P. A 1995 A new formulation of higher order Boussinesq equations. *COASTAL95, 6–8 Sept 1995, Cancun, Mexico.*

Stiassnie, M. & Kroszynski, U. I. 1982 Long-time evolution of an unstable water-wave train. *J. Fluid Mech.* **116**, 207–225.

Su, C. H. & Mirie, R. M. 1980 On head-on collisions between two solitary waves. *J. Fluid Mech.* **98**, 509–525.

Tanaka, M. 1986 The stability of solitary waves. *Phys. Fluids* **29**, 650–655.

Ting, F. C. K. & Kirby, J. T. 1994 Observation of undertow and turbulence in a laboratory surf zone. *Coastal Engng* **24**, 51–80.

Trulsen, K. & Dysthe, K. B. 1990 Frequency downshift through self modulation and breaking. In *Water Wave Kinematics* (ed. A. Tørum & O. T. Gudmestad), pp. 561–572. Kluwer.

Trulsen, K. & Dysthe, K. B. 1997 Frequency downshift in three-dimensional wave trains in a deep basin. *J. Fluid Mech.* **352**, 359–373.

Tulin, M. P. & Waseda, T. 1999 Laboratory observations of wave group evolution, including breaking effects. *J. Fluid Mech.* **378**, 197–232.

Tulin, M. P., Yao, Y. & Wang, P. 1994 The simulation of the deformation and breaking of ocean waves in wave groups. *BOSS'94, Boston, MA*, pp. 383–392.

Wei, G., Kirby, J. T., Grilli, S. T. & Subramanya, R. 1995 A fully nonlinear Boussinesq model for surface waves. Part 1. Highly nonlinear unsteady waves. *J. Fluid Mech.* **294**, 71–92.

Williams, J. M. 1985 *Tables of Progressive Gravity Waves.* Pitman.

Witting, J. M. 1984 A unified model for the evolution of nonlinear water waves. *J. Comput. Phys.* **56**, 203–236.

Wu, T. Y. 1995 Bidirectional soliton street. *Acta Mechanica Sinica* **11**(4), 289–306.

Wu, T. Y. 1998 Nonlinear waves and solitons in water. *Physica* D **123**, 48–63.

Wu, T. Y. 1999 Modeling nonlinear dispersive water waves. *J. Engng Mech.* **125**, 747–755.

Yamada, H. 1957 On the highest solitary wave. *Rep. Res. Inst. Appl. Mech., Kyushu Univ.*, **V**(18), 53–67.

Zakharov, V. E. 1968 Stability of periodic waves of finite amplitude on the surface of a deep fluid. *J. Appl. Mech. Tech. Phys.* **9**, 190–194.